An advanced regulatory control structure for the flexible operation of alkaline water electrolyzers in the day-ahead electricity market

Authors:

Lucas Cammann, Anushka Perera, Vidar Alstad, Johannes Jäschke

Date Submitted: 2025-10-16

Keywords: Hydrogen, Plantwide Control, Advanced Regulatory Control, Alkaline Water Electrolysis, HTO

Abstract:

To facilitate large-scale green hydrogen production, manufacturers are moving towards pressurized and strongly coupled topologies where multiple electrolyzers share the same processing equipment. This coupling increases the control challenges regarding temperature and safety-critical gas purity constraints. In this paper we develop two advanced regulatory control elements aimed at these constraints and embed them in a plantwide control structure for such systems. We show in dynamic simulations that our approach achieves nearly the same production efficiency as with an explicit optimization layer, while being inherently safer compared to reference control structures. We further show that it can extend the operating limits by up to 50% compared to simpler regulatory control layers, allowing for significant increases in flexibility and thereby profitability in the day-ahead electricity market.

Record Type: Preprint

Submitted To: LAPSE (Living Archive for Process Systems Engineering)

Citation (overall record, always the latest version):

Citation (this specific file, latest version):

LAPSE:2025.0720

LAPSE:2025.0720-1

Citation (this specific file, this version):

LAPSE:2025.0720-1v1

License: Creative Commons Attribution-NonCommercial-NoDerivatives 4.0 International (CC BY-NC-ND 4.0)

An advanced regulatory control structure for the flexible operation of alkaline water electrolyzers in the day-ahead electricity market

Lucas Cammann,[†] Anushka Perera,[‡] Vidar Alstad,[¶] and Johannes Jäschke*,[†]

†Department of Chemical Engineering, Norwegian University of Science and Technology, 7491 Trondheim, Norway

‡ Yara International ASA, Yara Technology and Projects, 3936 Porsgrunn, Norway ¶Hydro Aluminium AS, Technology and Operational Support, 3936 Porsgrunn, Norway

E-mail: johannes.jaschke@ntnu.no

Abstract

To facilitate large-scale green hydrogen production, manufacturers are moving towards pressurized and strongly coupled topologies where multiple electrolyzers share the same processing equipment. This coupling increases the control challenges regarding temperature and safetycritical gas purity constraints. In this paper we develop two advanced regulatory control elements aimed at these constraints and embed them in a plantwide control structure for such systems. We show in dynamic simulations that our approach achieves nearly the same production efficiency as with an explicit optimization layer, while being inherently safer compared to reference control structures. We further show that it can extend the operating limits by up to 50% compared to simpler regulatory control layers, allowing for significant increases in flexibility and thereby profitability in the day-ahead electricity market.

1 Introduction

Alkaline water electrolysis (AEL) is a mature technology for producing hydrogen (H_2) and oxygen (O_2) gas from water using electrical energy. First commercialized in the early 1900s, ¹ AEL has recently regained attention as a scal-

able method for generating hydrogen from renewable electricity, either via the grid or directly coupled sources. While early systems already utilized renewable energy in the form of hydropower,² modern deployments increasingly rely on intermittent sources like wind and solar. This shift introduces significant control challenges, with reports of large-scale plants requiring redesigns due to insufficient operational flexibility.³

The inherent control challenge in AEL lies in maintaining operation within manufacturerrated upper and lower load limits. These are governed by constraints on the temperature and current density (upper limit) and the gas purity (lower limit). A typically reported upper temperature limit is 80°C, beyond which efficiency improves but the corrosiveness of the lye increases. While exceeding this limit may not immediately compromise safety, it does impact longevity. In contrast, the lower load limit is critical for safety, as it affects the oxygento-hydrogen (OTH) and hydrogen-to-oxygen (HTO) ratios. These must remain below 2%, half of the lower explosion limit, to prevent the formation of explosive gas mixtures.⁴ At low loads, gas purity reduces due to lower production rates while cross-contamination mechanisms persist, increasing the relative concentration of undesired species. Key contamination pathways include diffusion and convection across cell membranes and mixing of anolyte and catholyte during lye rebalancing.^{4,5}

For a stand-alone, pressurized alkaline electrolyzer (called 1-in-1 configuration⁶), David et al. 7 used decoupled Proportional-Integral (PI) controllers and \mathcal{H}_{∞} control to control the HTO. Manipulated variables were the outlet valves of the anodic gas-liquid separator, and simulations were carried out on a high-fidelity model. The same model was later used by Uribe et al. 8 for sliding mode control. Qi et al. presented pressure control strategies taking into account HTO constraints using optimal curve tracking (OCT) control and model predictive control (MPC). The developed strategies were based on a dynamic model verified on a smallscale, 0.5 Nm³/h test system. Also using optimal curve tracking control, Li et al. 10 introduced lye flow rate control in addition to pressure control to reduce the lower operating limit. The control model was verified on a 4kW test system, and it was found that the lower operating limit could be reduced to 8.95\% compared to 11.78% using pressure control only and 20% with constant pressure operation. Hu et al. 11 similarly proposed a control strategy in which the pressure and lye flow rate are used synergistically in an OCT framework. The proposed strategy was tested on a 250 kW test system, where it was found to reduce the minimum load from 42% to 15.6%. Both the lye flow rate and the pressure have also been used by Cammann and Jäschke¹² in a purely feedback-based manner using PI-controllers with different setpoints. Comparatively fewer studies have been dedicated to alkaline electrolysis systems in which multiple electrolyzers are part of the same balance of plant (BoP), referred to as N-in-1 configurations. 6 Rizwan et al. 13 have investigated operating strategies for a weakly coupled system (electrolyzers sharing the same lye recirculation loop) using steady-state optimization. Their findings suggest that in such configurations, variable lye flow rate operation can increase the hydrogen production by 8-12%. Building on this model, Shi et al. 14 presented a dual-layer control strategy with a real-time optimization (RTO) layer and a control layer

utilizing both dynamic matrix control (DMC) and PID-control. Chen *et al.* ¹⁵ have presented a start-up strategy for weakly coupled systems using dynamic optimization to increase thermal efficiency.

In contrast to the aforementioned weakly coupled systems, strongly coupled systems share not only a common lye recirculation loop but also gas-liquid separation. These systems offer further cost reductions and are commonly adopted for large-scale projects on the scale of 100 MW. Zheng et al. ¹⁶ and Liang et al. ¹⁷ presented PID and rule-based control approaches for such systems. Li et al. ¹⁸ presented further rule-based strategies, while Qiu et al. ⁶ proposed a nonlinear MPC (nMPC) framework. While the former studies do not explicitly take HTO control into account, the latter does, however, neglecting the potential influence of the operating pressure.

The above studies show certain limitations. Firstly, control studies aiming to increase the load flexibility are almost exclusively done for simple 1-in-1 topologies. Of those considering strongly coupled configurations, no study presents a framework that addresses the simultaneous manipulation of the pressure and the lye flow rates to control the HTO. Secondly, studies that are concerned with the optimal operation of AEL systems typically employ model-based control methods. This increases the implementation burden and requires accurate models, delaying or hindering their industrial adaptation. Lastly, little attention is paid to the control of alkaline electrolysis systems under the flexibility constraints most likely to be imposed today, that is, in a grid-connected setting under participation in the day-ahead electricity market. Inspired by these research gaps, we herein aim to answer the following questions:

- Q.1 How can flexible process operation for alkaline water electrolyzers be facilitated using only simple control elements, and how does this compare to alternative control implementations?
- Q.2 What are the potential benefits of flexible

operation when participating in the dayahead electricity market?

To answer these questions, we present a dynamic plant model and an advanced regulatory control (ARC) structure coupled to a scheduling layer giving power setpoints to the plant. Importantly, the control structure uses only standard control elements to automatically switch between relevant operating regions. It is conceived using a systematic procedure following Skogestad and tested against a power profile based on historical electricity prices. Based on our results, we claim the following novelties:

- 1) Two advanced regulatory control elements are developed that allow to safely extend the load range of pressurized *N*-in-1 AEL systems.
- Based on these, we develop a plantwide advanced regulatory control structure for the operation in the day-ahead electricity market.
- 3) This control structure reaches nearly the efficiency possible using an optimization layer, while being inherently more robust towards unmodeled disturbances.

Regarding 1) and 2), we believe that it is relevant to rely as best possible on simple, modelfree control strategies given the difficulties of model generation and maintenance in industrial practice. Regarding 3), we note that the gas purity is highly safety-critical, calling for an extensive regulatory control logic in addition to any potential model-based control effort. It is hence desirable to design such logic as close to optimal as possible. The remainder of this paper is structured as follows. We introduce the dynamic plant model and its underlying assumption in Sec. 2. In Sec. 3 we present the developed advanced regulatory control elements that lay the foundation for the resulting plantwide control structure in Sec. 4. To answer the posed research questions, we formulate a case study, which is detailed in Sec. 5. Finally, we present the discussion and conclusions in Secs. 6 and 7.

2 Model development

The following section presents the dynamic plant model used in this work. The main equations are presented in tabular form for the sake of brevity, and we focus on presenting important mechanistic effects and highlighting relevant assumptions.

2.1 Plant layout

Three alkaline electrolyzers lie at the heart of the considered process plant, shown in Figure 1. The plant is strongly coupled, and hence all electrolyzers share the same lye recirculation, gas-liquid separators, and one common external voltage source. The voltage U gives rise to the applied current densities I in the electrolyzers, facilitating the following electrochemical reaction in the electrolysis cells

$$H_2O(l) \longrightarrow H_2(g) + \frac{1}{2}O_2(g).$$
 (1)

Here, H_2 is produced at the cathode and O_2 at the anode. The product gases are separated from the conductive aqueous lye (30% wt. aq. KOH) in two gas-liquid separators. The gaseous hydrogen effluent is pressurized to storage pressure, while the oxygen is vented. The remaining lye is recirculated and combined in a buffer tank. This serves to balance the concentration of ions in the lye and to replenish water consumed in the electrolysis reactions. The lye from the buffer tank is pressurized, cooled through a heat exchanger and then resupplied to the electrolysis stacks.

The governing equations for the plant can be found in Table 1. Here, differential equations are collected as $f(\cdot)$, algebraic equations as $g(\cdot)$ and operational inequality constraints as $h(\cdot)$. Equations are abstracted by using sets $\mathcal{K} = \{1, 2, 3\}$ for the connected electrolyzers, $\mathcal{J} = \{H_2, O_2\}$ for the gaseous species, and $\mathcal{S} = \{a, c\}$ for the anode and cathode sides. Additional sources, parameter values, or further derivations can be found in the App. B.

2.2 Electrolyzer

Each electrolyzer has a nominal capacity of $2.135\,\mathrm{MW}$ and is composed of $n_\mathrm{c}=230$ in-

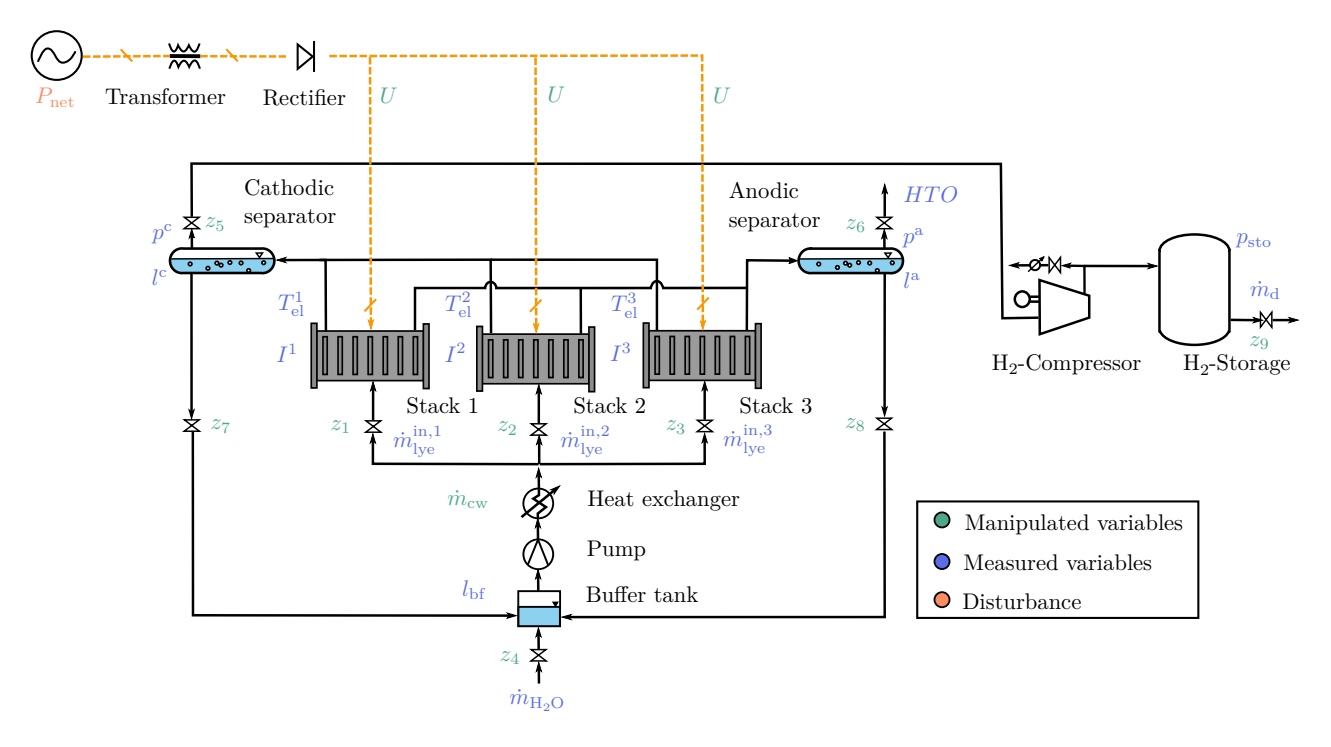


Figure 1: Plant layout for the strongly coupled alkaline water electrolysis plant. Green text shows manipulated variables, blue text control variables, and orange text disturbances.

dividual cells connected in a bipolar fashion. The dynamic energy balance (Eq. 1a) follows Rizwan et al., while the relationship between the applied voltage U, the current densities Iand temperatures $T_{\rm el}$ in the electrolyzers follows the commonly used Ulleberg model (Ulleberg, Eq. 1c). We additionally consider the bubble coverage effects through two overvoltage terms $\Delta \eta_{o,\theta}$ and $\Delta \eta_{act,\theta}$ (Cammann *et al.*, Eqs. 1d to 1g). Mass balances are formulated in terms of algebraic component balances (Eq. 1j) for the gaseous species and an overall mass balance (Eq. 1m). The reaction term follows Faraday's law, accounting for the faradaic efficiency, 20 whereas the diffusion across the membrane follows Fick's law (Eq. 11), for which we assume the driving force is equal to the saturation concentration. Temperatures in the electrolyzers are limited to 80 °C, while the lye flow rate through each electrolyzer is constrained between 1 kg s^{-1} and 10 kg s^{-1} (Eqs. 10 to 1q).

2.3 Gas-liquid separators

As the equations for the two separators are conceptually identical, both are abstracted by the use of superscripts c (catholyte) and a

(anolyte). Each separator is equally sized to allow for a liquid residence time of $\approx 2 \,\mathrm{min}$ at the highest lye flow rate. For a conservative estimate of the gas impurity, we assume that this allows the foreign gas species (H₂ at the anode side and O_2 at the cathode side) to leave the separators entirely through the gas phase (Eqs. 2f and 2g). To ensure safe process operation, the $HTO = x_{\rm H_2}^a/x_{\rm O_2}^a$ must be below 2 % (Eq. 2i). As shown in Figure 1 the HTO is measured at the outlet of the gas-liquid separator, as current measurement devices require a pure gas phase. In order to reduce pressuredriven gas crossover, the pressure difference between the two separators must be contained below 0.15 bar (Eq. 2j).

2.4 Recycle

The buffer tank, pump, and the heat exchanger comprise the recycle system. Lumped energy balances are considered for the buffer tank (Eq. 3c) and the heat exchanger (Eqs. 3d and 3e), with the logarithmic temperature difference T_{log} (Eq. 3f) being used as effective temperature difference in the latter.

Table 1: Governing equations for strongly coupled alkaline water electrolysis system. Differentials $\frac{d()}{dt}$ on the right hand side are shortened as ()'.

		Electrolyzer equations		Remark
$f(\cdot)$		$A_{\rm el}(U^k - U_{\rm tn})I^k + \dot{m}_{\rm lye}^{\rm in,k}Cp_{\rm l}(T_{\rm el}^{\rm in} - T_{\rm el}^k) + A_{\rm s}(h_{\rm c}(T_{\rm el}^k - T_{\rm a}) + \sigma\epsilon(T_{\rm el}^{k^4} - T_{\rm a}^4))$	(1a)	$^{13} k \in \mathcal{K}$
$g(\cdot)$		$U_{\rm rev}^k/[V] - 1.518 + 1.5421 \times 10^{-3} T_{\rm el}^k - 9.523 \times 10^{-5} T_{\rm el}^k \ln(T_{\rm el}^k) - 9.84 \times 10^{-8} T_{\rm el}^{k^2}$	(1b)	22 $k \in \mathcal{K}$
	0 =	$\eta^k - s^k \log_{10} \left(\left(t_1 + \frac{t_2}{(T_{ m el}^k)^{\circ} m C)} + \frac{t_3}{(T_{ m el}^k)^{\circ} m C)^2} \right) I^k + 1 \right) - r_1^k - r_2 (T_{ m el}^k)^{\circ} m C) I^k$	(1c)	20 $k \in \mathcal{K}$
			(1d)	21 $k \in \mathcal{K}$
	0 =	$ \Delta \eta_{\text{o},\theta}^k - \frac{d_e I^k}{\kappa} \left((1 - 2\theta_0^k/3)^{-1.5} - (1 - 2\theta^k/3)^{-1.5} \right) \\ \Delta \eta_{\text{act},\theta}^k - 2.306RT_{\text{el}}^k \left(\log(1 - \theta^k) - \log(1 - \theta_0^k) \right) / (2F) $	(1e)	21 $k \in \mathcal{K}$
	0 =	$\theta_0^k - (I^k/I_{\theta \to 1})^{\mathrm{m}}$	(1f)	21,23 $k \in \mathcal{K}$
	0 =	$ heta^k - heta_0^k igl(1 + (K \dot{m}_{ m lye}^{ m in,k}/(ho n_{ m c} A_{ m f}))^2igr)^2$	(1g)	21,24 $k \in \mathcal{K}$
	0 =	$\lambda_{\mathrm{F}}^k - f_2^k I^{k^2} / (f_1^k + I^k^2)$ $U^k - U_{\mathrm{rev}}^k - \eta^k + \Delta \eta_{\mathrm{o}, \theta}^k + \Delta \eta_{\mathrm{act}, \theta}^k$	(1h)	$k \in \mathcal{K}$
	0 =	$U^k - U^k_{ m rev} - \eta^k + \Delta \eta^k_{ m o, heta} + \Delta \eta^k_{ m act, heta}$	(1i)	$^{21} k \in \mathcal{K}$
	0 =	$0.5 \dot{n}_{\mathrm{el},j}^{\mathrm{in},k} + \dot{n}_{\mathrm{r},j}^k \pm \dot{n}_{\mathrm{diff},j}^k - \dot{n}_{j}^{\mathrm{out},k,s}$	(1j)	$s \in \mathcal{S}, j \in \mathcal{J}, k \in \mathcal{K}$
	0 = 0	$\dot{n}_{\mathrm{r},j}^k - \lambda_{\mathrm{F}}^k I^k A_{\mathrm{el}}/(z_j F)$	(1k)	$j \in \mathcal{J}, k \in \mathcal{K}$
	0 =	$n_{\text{diff},j}^{k} - p\rho_{\text{I}}S_{j}D_{j}A_{\text{el}}/d_{\text{m}}$	(1l)	$j \in \mathcal{J}, k \in \mathcal{K}$
	0 =	$\sum_{j \in \mathcal{J}} M_j (n_{\mathrm{el},j}^{\mathrm{in},n} - n_j^{\mathrm{ott},n,s}) + m_{\mathrm{lye}}^{\mathrm{in},n} - m_{\mathrm{lye}}^{\mathrm{ott},n}$	(1m)	$k \in \mathcal{K}$
h()	0 =	$ \begin{aligned} $	(1n)	$h \in \mathcal{K}$
$h(\cdot)$	0 <	$10 \mathrm{kg} \mathrm{s}^{-1} - \dot{m}_{\mathrm{lye}}^{\mathrm{in},k}$	(1o) (1p)	$k \in \mathcal{K}$ $k \in \mathcal{K}$
	0 <	$\dot{m}_{ m lye}^{ m in} = 1 { m kg} { m s}^{-1}$	(1p) (1q)	$k \in \mathcal{K}$ $k \in \mathcal{K}$
Type	0 \(\)	M _{lye} - 1 kg s Separator equations	(1q)	Remark
	$\mathrm{d} p^s$		(0.)	
$f(\cdot)$	$\frac{\overline{\mathrm{d}}t}{\mathrm{d}V_{\mathrm{l}}^{s}}=$	$\begin{split} & \left(R\tilde{T}(\sum_{k \in \mathcal{K}} \dot{n}_{j}^{\text{out},k,s} + \dot{n}_{i \neq j,\text{g}}^{\text{in},s} + \dot{n}_{\text{g}}^{\text{out},s}) + p^{s}(V_{\text{l}}^{s})'\right)/V_{\text{g}}^{s} \\ & \left(0.5 \sum_{k \in \mathcal{K}} \dot{m}_{\text{lye}}^{\text{out},k} - \dot{m}^{\text{out},s}\right)/\rho_{\text{l}} \\ & R\tilde{T}(x_{i}^{s} \dot{n}_{j,\text{g}}^{\text{in},s} - x_{j}^{s} \sum_{k \in \mathcal{K}} \dot{n}_{i}^{\text{out},s})/(pV_{\text{g}}^{s}) \\ & \left(\dot{n}_{j,\text{l}}^{\text{in}} - c_{j}^{s}/(2\rho \sum_{k \in \mathcal{K}} \dot{m}^{\text{out},k})\right)/V_{\text{l}}^{s} \end{split}$	(2a)	$s, j = \{a, O_2\} \lor \{c, H_2\}$
	$\frac{1}{\mathrm{d}t} =$	$(0.5 \sum_{k \in \mathcal{K}} m_{\text{lye}} - m^{\text{out, 5}})/\rho_{\text{l}}$	(2b)	$s \in \mathcal{S}$
	$\frac{dt}{dt^s} =$	$R\tilde{T}(x_i^s \dot{n}_{j,\mathrm{g}}^{\mathrm{in},s} - x_j^s \sum_{\mathrm{k} \in \mathcal{K}} \dot{n}_i^{\mathrm{out},s})/(pV_{\mathrm{g}}^s)$	(2c)	$s \in \mathcal{S}, j \neq i \in \mathcal{J}$
	$\frac{\mathrm{d} c_j}{\mathrm{d} t} =$	$ig(\dot{n}_{j,\mathrm{l}}^{\mathrm{in}} - c_{j}^{s}/(2 ho\sum_{k\in\mathcal{K}}\dot{m}_{\mathrm{lye}}^{\mathrm{out},k})ig)/V_{\mathrm{l}}^{s}$	(2d)	$s, j = \{a, \mathcal{O}_2\} \vee \{c, \mathcal{H}_2\}$
$g(\cdot)$	0 =	$V_{ m sep} - V_{ m g}^s - V_{ m l}^s = V_{ m l}^s$ $\sum_{{f k} \in \mathcal{K}} \dot{n}_j^{{ m out},k,s} - \dot{n}_{j,{ m l}}^{{ m in},s} - \dot{n}_{j,{ m g}}^{{ m in},s}$	(2e)	$s \in \mathcal{S}$
	0 =	$\sum_{\mathbf{k} \in \mathcal{K}} n_j^{\text{rad},\gamma,\gamma} - n_{j,1}^{\text{rad}} - n_{j,g}^{\text{rad}}$	(2f)	$s, j = \{a, O_2\} \lor \{c, H_2\}$
	0 =	$\begin{array}{l} \sum_{\mathbf{k} \in \mathcal{K}} \gamma_{j,1} & \gamma_{j,\mathrm{g}} \\ \dot{n}_{j,1}^{\mathrm{in},s} - \dot{m}^{\mathrm{out},s} S_{j} p / \lambda_{\mathrm{sep}} \\ \widetilde{T}_{\mathrm{m}} - (\sum_{k \in \mathcal{K}} T_{\mathrm{l}k}^{\mathrm{i}} \dot{m}_{\mathrm{lye}}^{\mathrm{out},k}) / (\sum_{k \in \mathcal{K}} \dot{m}_{\mathrm{lye}}^{\mathrm{out},k}) \end{array}$	(2g)	$s, j = \{a, O_2\} \vee \{c, H_2\}$
1()	0 =	$T_{\rm m} - (\sum_{k \in \mathcal{K}} T_{\rm el}^{\kappa} m_{\rm lye}^{\rm max, s}) / (\sum_{k \in \mathcal{K}} m_{\rm lye}^{\rm max, s})$	(2h)	Ct : t . 1 . 1: : t
$h(\cdot)$	$0 \le 0 < 0$	HTO - 0.02 $0.15 \mathrm{bar} - p^{\mathrm{a}} - p^{\mathrm{c}} $	(2i) (2j)	Strict alarm limit
Type	0 ≥	Recycle equations	(2J)	Remark
	dese		/- \	
$f(\cdot)$	$\frac{\frac{\mathrm{d}c_{\mathrm{bf},j}}{\mathrm{d}t}}{\frac{\mathrm{d}V_{\mathrm{bf}}}{\mathrm{d}t}} =$	$(c_j^s \dot{m}^{\text{out},s}/\rho_l - \sum_{\mathbf{k} \in \mathcal{K}} \dot{n}_{\mathrm{el},j}^{\mathrm{in},k} - c_{\mathrm{bf},j} V_{\mathrm{bf}}')/V_{\mathrm{bf}}$	(3a)	$s, j = \{a, \mathcal{O}_2\} \vee \{c, \mathcal{H}_2\}$
	$\frac{\mathrm{d} r_{\mathrm{bf}}}{\mathrm{d} t} =$	$(\sum_{s \in \mathcal{S}} \dot{m}^{\text{out},s} + \dot{m}^{\text{in}}_{\text{bf},\text{H}_2\text{O}} - \sum_{k \in \mathcal{K}} \dot{m}^{\text{in},k}_{\text{lye}})/\rho_1$	(3b)	
	$\frac{\mathrm{d}T_{\mathrm{bf}}}{\mathrm{d}t} =$	$(\sum_{k \in \mathcal{K}} \dot{m}_{\mathrm{lye}}^{\mathrm{out},k} (\tilde{T}_{\mathrm{m}} - T_{0}) - (T_{\mathrm{bf}} - T_{0}) (\sum_{k \in \mathcal{K}} \dot{m}_{\mathrm{lye}}^{\mathrm{in},k} + \rho_{\mathrm{l}} V_{\mathrm{bf}}') / (\rho_{\mathrm{l}} V_{\mathrm{bf}})$	(3c)	10
	$\frac{\mathrm{d}T_{\mathrm{el}}^{\mathrm{in}}}{\mathrm{d}t} =$	$\left(\sum_{k\in\mathcal{K}}\dot{m}_{\mathrm{lye}}^{\mathrm{in},k}Cp_{\mathrm{l}}(T_{\mathrm{bf}}-T_{\mathrm{el}}^{\mathrm{in}})-\mathrm{UHX}T_{\mathrm{log}} ight)/(m_{\mathrm{hs}}Cp_{\mathrm{l}})$	(3d)	13
	dt			
	$\frac{\mathrm{d}T_{\mathrm{cw}}^{\mathrm{out}}}{\mathrm{d}t} =$		(3e)	13
$g(\cdot)$	$\frac{\mathrm{d}T_{\mathrm{cw}}^{\mathrm{out}}}{\mathrm{d}t} = 0$		(3f)	
	$\frac{\mathrm{d}T_{\mathrm{cw}}^{\mathrm{out}}}{\mathrm{d}t} = 0$ $0 = 0$	$ \begin{array}{l} \left(\dot{m}_{\rm cw}^{\rm in} C p_{\rm H_2O}(T_{\rm cw} - T_{\rm cw}^{\rm out}) + {\rm UHX} T_{\rm log}\right) / (m_{\rm cs} C p_{\rm H_2O}) \\ T_{\rm log} - \left((T_{\rm bf} - T_{\rm cw}^{\rm out}) - (T_{\rm el}^{\rm in} - T_{\rm cw})\right) / \log\left((T_{\rm bf} - T_{\rm cw}^{\rm out}) / (T_{\rm el}^{\rm in} - T_{\rm cw})\right) \\ \dot{n}_{\rm el,j}^{\rm in,k} - \dot{m}_{\rm lve}^{\rm in,k} c_{\rm bf,j} \end{array} $	(3f) (3g)	$k \in \mathcal{K}, j \in \mathcal{J}$
$g(\cdot)$ $h(\cdot)$	$\frac{\mathrm{d}T_{\mathrm{cw}}^{\mathrm{out}}}{\mathrm{d}t} = 0$	$ \begin{array}{l} \left(\dot{m}_{\rm cw}^{\rm in} C p_{\rm H_2O}(T_{\rm cw} - T_{\rm cw}^{\rm out}) + {\rm UHX} T_{\rm log}\right) / (m_{\rm cs} C p_{\rm H_2O}) \\ T_{\rm log} - \left((T_{\rm bf} - T_{\rm cw}^{\rm out}) - (T_{\rm el}^{\rm in} - T_{\rm cw})\right) / \log\left((T_{\rm bf} - T_{\rm cw}^{\rm out}) / (T_{\rm el}^{\rm in} - T_{\rm cw})\right) \\ \dot{n}_{\rm el,j}^{\rm in,k} - \dot{m}_{\rm lye}^{\rm in,k} c_{\rm bf,j} \\ 80 {\rm kg s^{-1}} - \dot{m}_{\rm cw} \end{array} $	(3f)	
$\frac{h(\cdot)}{\text{Type}}$	$\frac{\mathrm{d}T_{\mathrm{cw}}^{\mathrm{out}}}{\mathrm{d}t} = 0 = 0 = 0 \leq$	$ \frac{(\dot{m}_{\rm cw}^{\rm in} C p_{\rm H_2O}(T_{\rm cw} - T_{\rm cw}^{\rm out}) + {\rm UHX} T_{\rm log})/(m_{\rm cs} C p_{\rm H_2O})}{T_{\rm log} - \left((T_{\rm bf} - T_{\rm cw}^{\rm out}) - (T_{\rm el}^{\rm in} - T_{\rm cw})\right)/\log\left((T_{\rm bf} - T_{\rm cw}^{\rm out})/(T_{\rm el}^{\rm in} - T_{\rm cw})\right)}{\dot{n}_{\rm el,j}^{\rm in,k} - \dot{m}_{\rm lye}^{\rm in,k} c_{\rm bf,j}}{80{\rm kgs^{-1}} - \dot{m}_{\rm cw}} $ Storage equations	(3f) (3g)	
$\frac{h(\cdot)}{\text{Type}}$	$\frac{\mathrm{d}T_{\mathrm{cw}}^{\mathrm{out}}}{\mathrm{d}t} = 0 = 0 = 0 \leq \frac{\mathrm{d}p_{\mathrm{sto}}}{\mathrm{d}t} = 0$	$ \frac{(\dot{m}_{\rm cw}^{\rm in} C p_{\rm H_2O}(T_{\rm cw} - T_{\rm cw}^{\rm out}) + {\rm UHX} T_{\rm log})/(m_{\rm cs} C p_{\rm H_2O})}{T_{\rm log} - \left((T_{\rm bf} - T_{\rm cw}^{\rm out}) - (T_{\rm el}^{\rm in} - T_{\rm cw})\right)/\log\left((T_{\rm bf} - T_{\rm cw}^{\rm out})/(T_{\rm el}^{\rm in} - T_{\rm cw})\right)}{\log\left((T_{\rm bf} - T_{\rm cw}^{\rm out})/(T_{\rm el}^{\rm in} - T_{\rm cw})\right)} $ $ \frac{\dot{n}_{\rm el,j}^{\rm in,k} - \dot{m}_{\rm lye}^{\rm in,k} c_{\rm bf,j}}{80 {\rm kg s^{-1}} - \dot{m}_{\rm cw}} $ Storage equations $ R\tilde{T}_{\rm m} \left(\sum_{k \in \mathcal{K}} \dot{n}_{\rm r,H_3}^k - \dot{n}_{\rm H_3}^{\rm out}\right)/V_{\rm sto} $	(3f) (3g) (3h) (4a)	$k \in \mathcal{K}, j \in \mathcal{J}$
$\frac{h(\cdot)}{\text{Type}}$ $f(\cdot)$ $g(\cdot)$	$\frac{dT_{\text{cut}}^{\text{cut}}}{dt} = 0$ $0 = 0$ $0 \le \frac{dp_{\text{sto}}}{dt} = 0$ $0 = 0$	$\begin{split} & (\dot{m}_{\rm cw}^{\rm in} C p_{\rm H_2O}(T_{\rm cw} - T_{\rm cw}^{\rm out}) + {\rm UHX} T_{\rm log})/(m_{\rm cs} C p_{\rm H_2O}) \\ & T_{\rm log} - \left((T_{\rm bf} - T_{\rm cw}^{\rm out}) - (T_{\rm el}^{\rm in} - T_{\rm cw}) \right)/\log\left((T_{\rm bf} - T_{\rm cw}^{\rm out})/(T_{\rm el}^{\rm in} - T_{\rm cw}) \right) \\ & \dot{n}_{\rm el,j}^{\rm in,k} - \dot{m}_{\rm lye}^{\rm in,k} c_{\rm bf,j} \\ & 80 {\rm kg s^{-1}} - \dot{m}_{\rm cw} \end{split}$ Storage equations $& R \tilde{T}_{\rm m} (\sum_{{\bf k} \in \mathcal{K}} \dot{n}_{\rm r,H_2}^k - \dot{n}_{\rm H_2}^{\rm out})/V_{\rm sto} \\ & P_{\rm co} - \sum_{{\bf k} \in \mathcal{K}} \dot{n}_{\rm r,H_2}^k \gamma/(\lambda_{\rm co}(\gamma - 1)) R \tilde{T} \left((p_{\rm sto}/p)^{(\gamma - 1)/\gamma} - 1 \right) \end{split}$	(3f) (3g) (3h) (4a) (4b)	$k \in \mathcal{K}, j \in \mathcal{J}$
$\frac{h(\cdot)}{\text{Type}}$	$\frac{\mathrm{d}T_{\mathrm{cut}}^{\mathrm{cut}}}{\mathrm{d}t} = 0 = 0 = 0 \leq \frac{\mathrm{d}p_{\mathrm{sto}}}{\mathrm{d}t} = 0 = 0 \leq 0 \leq 0 \leq 0 = 0 \leq 0 \leq 0$	$\begin{split} & (\dot{m}_{\rm cw}^{\rm in} C p_{\rm H_2O}(T_{\rm cw} - T_{\rm cw}^{\rm out}) + {\rm UHX} T_{\rm log})/(m_{\rm cs} C p_{\rm H_2O}) \\ & T_{\rm log} - \left((T_{\rm bf} - T_{\rm cw}^{\rm out}) - (T_{\rm el}^{\rm in} - T_{\rm cw}) \right)/\log\left((T_{\rm bf} - T_{\rm cw}^{\rm out})/(T_{\rm el}^{\rm in} - T_{\rm cw}) \right) \\ & \dot{n}_{\rm el,j}^{\rm in,k} - \dot{m}_{\rm lye}^{\rm in,k} c_{\rm bf,j} \\ & 80{\rm kgs^{-1}} - \dot{m}_{\rm cw} \end{split}$ Storage equations $& R\tilde{T}_{\rm m} \left(\sum_{{\bf k} \in \mathcal{K}} \dot{n}_{\rm r,H_2}^k - \dot{n}_{\rm H_2}^{\rm out} \right)/V_{\rm sto} \\ & P_{\rm co} - \sum_{{\bf k} \in \mathcal{K}} \dot{n}_{\rm r,H_2}^k \gamma/\left(\lambda_{\rm co}(\gamma-1)\right) R\tilde{T}\left((p_{\rm sto}/p)^{(\gamma-1)/\gamma} - 1 \right) \\ & p_{\rm sto} - 30{\rm bar} \end{split}$	(3f) (3g) (3h) (4a) (4b) (4c)	$k \in \mathcal{K}, j \in \mathcal{J}$
$\frac{h(\cdot)}{\text{Type}}$ $f(\cdot)$ $g(\cdot)$	$\frac{dT_{\text{cut}}^{\text{cut}}}{dt} = 0$ $0 = 0$ $0 \le \frac{dp_{\text{sto}}}{dt} = 0$ $0 = 0$	$\begin{split} & (\dot{m}_{\rm cw}^{\rm in} C p_{\rm H_2O}(T_{\rm cw} - T_{\rm cw}^{\rm out}) + {\rm UHX} T_{\rm log})/(m_{\rm cs} C p_{\rm H_2O}) \\ & T_{\rm log} - \left((T_{\rm bf} - T_{\rm cw}^{\rm out}) - (T_{\rm el}^{\rm in} - T_{\rm cw}) \right)/\log\left((T_{\rm bf} - T_{\rm cw}^{\rm out})/(T_{\rm el}^{\rm in} - T_{\rm cw}) \right) \\ & \dot{n}_{\rm el,j}^{\rm in,k} - \dot{m}_{\rm lye}^{\rm in,k} c_{\rm bf,j} \\ & 80 {\rm kg s^{-1}} - \dot{m}_{\rm cw} \end{split}$ Storage equations $& R \tilde{T}_{\rm m} (\sum_{{\bf k} \in \mathcal{K}} \dot{n}_{\rm r,H_2}^k - \dot{n}_{\rm H_2}^{\rm out})/V_{\rm sto} \\ & P_{\rm co} - \sum_{{\bf k} \in \mathcal{K}} \dot{n}_{\rm r,H_2}^k \gamma/(\lambda_{\rm co}(\gamma - 1)) R \tilde{T} \left((p_{\rm sto}/p)^{(\gamma - 1)/\gamma} - 1 \right) \end{split}$	(3f) (3g) (3h) (4a) (4b)	$k \in \mathcal{K}, j \in \mathcal{J}$

We assume constant hold-ups on the hot and cold side of the heat exchanger ($m_{\rm hs}$ and $m_{\rm cs}$), with the maximum cooling water flow rate $\dot{m}_{\rm cw}$ being $80 \, {\rm kg \, s^{-1}}$ (Eq. 3h)

2.5 Compression, storage, and pressure drops

The capacity of the H_2 storage tank V_{sto} is $200 \,\mathrm{m}^3$. The operating range of the system is constrained by upper and lower bounds on the pressures in the gas-liquid separators p^s and the storage tank p_{sto} . The minimum pressure in the storage tank is determined by delivery requirements for the hydrogen gas (30 bar), whereas the maximum pressure is determined assuming that a maximum compression ratio of 9 can be achieved (Eqs. 4c and 4d). Operating pressures for the electrolyzers effectively lie between 7.5 bar and 15 bar (Eqs. 4e and 4f).

Remaining equations not presented in Table 1 pertain to pressure drops and actuator dynamics in the system. For simplicity, we assume linear valve characteristics and that actuator positions z_i follow first order dynamics following the control signal. These aspects are further detailed in App. C.1.

3 Control element synthesis

We present two advanced regulatory control elements that were developed during the conception of the plantwide control structure. We explain them here in a more general setting to motivate their use outside of the application shown later.

3.1 Constraint-tracking override with integral reset controller

Override control is commonly used to comply with safety constraints and typically involves selector logic to choose the most conservative amongst several control signals. Figure 2a shows such logic with an override controller C1. For safety-critical variables we propose to add a second override controller, C2, with the

following control law:

$$u(t) = K_{\rm p} \left(-y(t) + \frac{1}{T_{\rm i}} \int_{\rm t_r}^{\rm t} e(\tau) d\tau \right) \text{ with }$$
 (5)

$$t_{\rm r}(t) = \max\{t_{\rm i} \le t | \operatorname{condition}(t_{\rm i}) = \mathtt{true}\}.$$
 (6)

This is a two-degree-of-freedom (2-DOF) PI controller with the following characteristics:

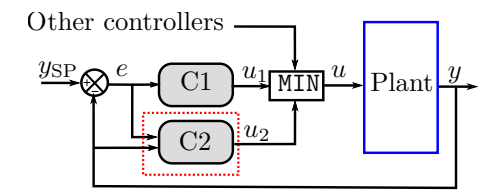
- 1. Setpoint weighting equal to zero for the proportional term (Eq. 5).
- 2. A condition for the reset of the integrated error at time $t_{\rm r}$ based on a disturbance measurement or proxy (Eq. 6).

This internal logic is shown in Figure 2b. The first characteristic minimizes the potential overshoot when approaching the constraint, while the second ensures that we do so starting from the most conservative control output.

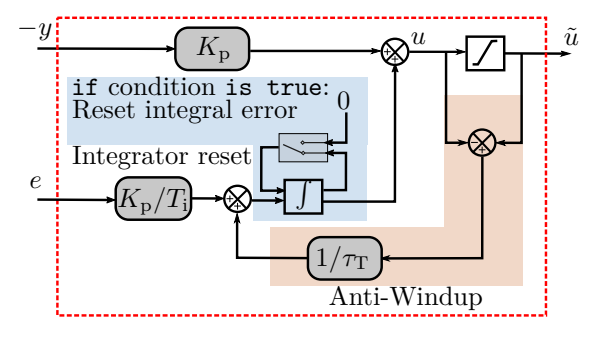
To illustrate this, we consider the following linear system for which we require $y \leq y_{\text{max}} = 1$.

$$y(s) = \underbrace{\frac{0.5}{100s+1}}_{G(s)} u(s) + \underbrace{\frac{1}{100s+1}}_{G_{d}(s)} d(s).$$
 (7)

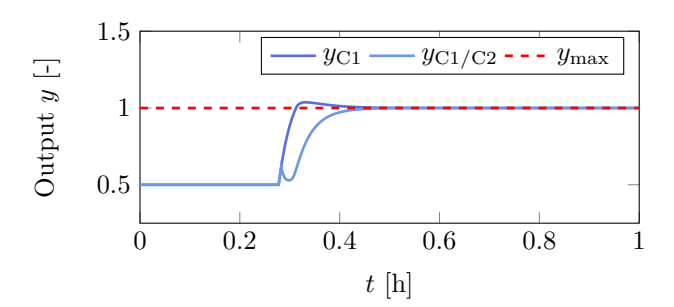
Figure 2c shows simulation results of the override system consisting of only C1, or C1 combined with C2 as shown in Figure 2a. Both controllers are tuned equally following SIMC rules²⁵ and we consider a disturbance d = 0.7entering the system at $t = 1000 \,\mathrm{s}$. Using only C1 gives an overshoot of 3.7% above the safety limit and would therefore require a backoff from the constraint. No overshoot occurs when using C2, and once the condition $d \ge 0.1$ is triggered, its integral error is reset and the controller output drops to 0. More important than the reduction in overshoot is the fact that this allows us to safely approach the new steady-state from a safe region, i.e., starting from the lowest possible input value. We will show later that this is particularly important for the control of the HTO, where the measurement of critical conditions might be delayed by several minutes.

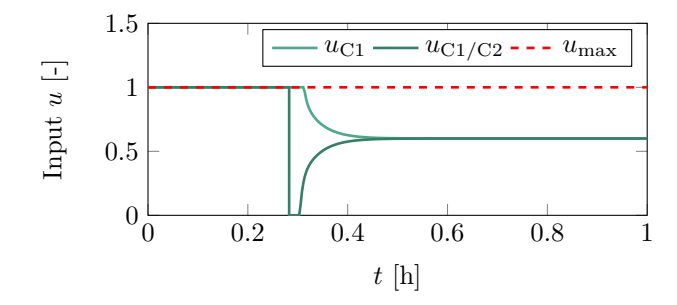


(a) Block diagram containing an override controller with integral reset (C2, marked as red) in addition to a conventional override controller C1.



(b) Block diagram of contstraint tracking override controller with integral reset logic.





(c) Disturbance step responses of the output y (upper), and the input u (lower) for the test system considering conventional override control and override control with an added constraint-tracking integral reset controller.

Figure 2: Override control structure (a), constraint-tracking override controller with integral reset (b) and disturbance step responses considering only conventional override control and an additional constraint-tracking integral reset controller (c).

3.2 Hierarchical override with input resetting

Figure 3 shows a second control structure, which we name "hierarchical override with input resetting" (HOIR). We consider systems with multiple parallel units i (here, i = 2) that share one common utility (here, u_1) and for which we desire to control the same process variables y_i . The shared utility has the largest gain on these variables, and each unit has individual inputs, which should be nominally high or low and can also affect said variable. The control structure is hierarchical as we select the shared utility to control the y_i with the largest constraint violation. The inputs u_i are then used to control the remaining y_i and reset to their nominal value once the disturbance is removed.

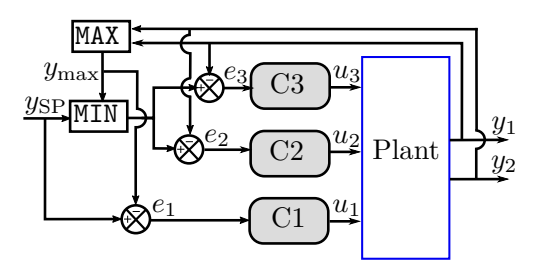


Figure 3: Block diagram of hierarchical override with input resetting.

4 Control structure development

The following section presents the development of the advanced regulatory control structure for the water electrolysis plant. Prior to this, we briefly discuss the overall control objective and the scheduling layer, which determines the powers at which the plant is operating.

4.1 Control objective and hierarchy

We consider operation given known day-ahead electricity prices $p_{\rm t}$, a constant demand $\dot{m}_{\rm d}$, and hourly changing production rates $\dot{m}_{\rm t}^{\rm prod}$. The objective function over a 24-hour time window \mathcal{T} may generally be written as the difference of the electricity cost $J_{\rm cost}$, ramp-up cost $J_{\rm ru}$ and the accrued profit $J_{\rm prof}$: ²⁶

$$\min_{\mathbf{z}, \mathbf{P}} \sum_{\mathbf{t} \in \mathcal{T}} \underbrace{p_{\mathbf{t}} P_{\mathrm{net}, \mathbf{t}}}_{\mathbf{J}_{\mathrm{cost}}} + \underbrace{p_{\mathrm{ru}} \mathbf{z}_{\mathbf{t}}^{\mathrm{ru}}}_{\mathbf{J}_{\mathrm{ru}}} - \underbrace{\dot{m}_{\mathbf{t}}^{\mathrm{prod}} p_{\mathrm{H}_{2}}}_{\mathbf{J}_{\mathrm{prof}}}. \tag{8}$$

Here, t are the hours for which the day-ahead prices are known, and P_t represents the scheduled power during these hours. Binary variables z designate in which state the electrolyzers operate (on, off, or standby), and we penalize ramp-ups from a cold state (\mathbf{z}^{ru}) . 26,27 It is assumed that the settling time for the system to reach steady-state is small compared to the hourly time window, introducing a timescale separation. This motivates the use of a twolayer approach, which is highlighted in Figure 4 as part of a general control hierarchy. Note that this approach does not rely on setpoint updates from a local optimization layer using, e.g., RTO. Instead, our aim is to develop the control layer to achieve safe and near-optimal operation given only new power setpoints $P_{\rm SP}$ from the scheduling layer and without the use of model-based control methods. For consistency, this approach then requires the scheduling layer to be informed not only about electricity price signals but also the efficiency η , as well as the minimum and maximum powers $(P_{\min} \text{ and } P_{\max})$ achievable with the control layer. We focus our attention going forward towards the development of the control layer; a full description of the optimization model employed in the scheduling layer can be found in App. A.

4.2 Control layer

The control layer consists of the supervisory and regulatory control layer. The task of the control layer is to stabilize the process to its economically optimal operating point given an external disturbance d, which we herein assume

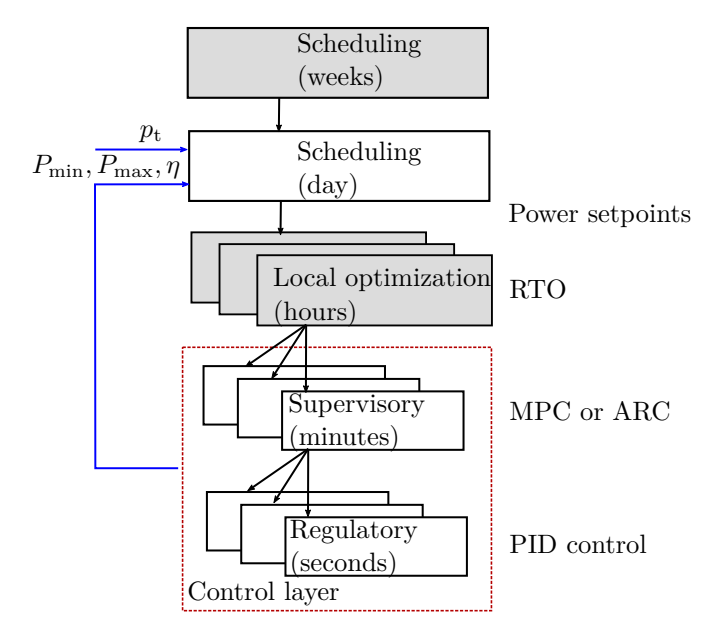


Figure 4: Depiction of a typical control hierarchy. Greyed out boxes are layers which are not considered in our approach, exogenous input signals to the scheduling layer are highlighted in blue.

to be the scheduled power P_{net} .

To this end, we follow in large part the principles outlined in ¹⁹ and adopt the following top-down procedure:

- 1. Define operational objective (cost) and constraints
- 2. Optimize degrees of freedom for disturbances
- 3. Implement optimal operation
- 4. Choose where to set production rate

We present these steps by summarizing related points for the sake of brevity.

4.2.1 Steps 1 & 2: Steady-state optimization

The steady-state optimization procedure follows that presented in Cammann *et al.*. Here, the following optimization problem is posed for a given power P_{net}

$$\max_{\mathbf{u}} \quad \dot{n}_{\mathrm{H}_{2}} \tag{9}$$
s.t. $f(\cdot) = 0$

$$g(\cdot) = 0$$

$$h(\cdot) \leq 0,$$

where the equality constraints $f(\cdot)$ and $g(\cdot)$ and the inequality constraints $h(\cdot)$ are written out as shown in Table 1.

In Eq. 9 u refers to the following setpoints

$$\mathbf{u} = [p^{\mathbf{a}}, \dot{m}_{\mathrm{cw}}, \dot{m}_{\mathrm{lye}}^{\mathrm{in}, 1}, \dot{m}_{\mathrm{lye}}^{\mathrm{in}, 2}, \dot{m}_{\mathrm{lye}}^{\mathrm{in}, 3}]. \tag{10}$$

We assume that the power consumption of the

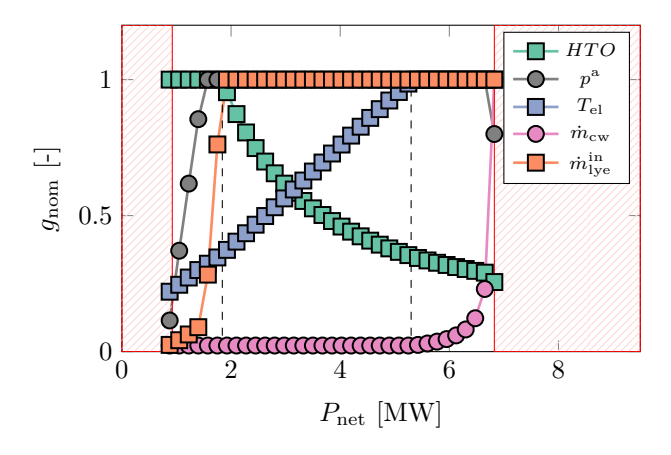


Figure 5: Normalized constraint value g_{nom} of relevant process variables given varying power inputs. Red regions indicate operating limits of the undegraded system. For clarity, regions are separated by dashed lines.

electrolyzers and compressor follows from the power and pressure setpoints and is not a degree of freedom. The optimization problem is solved for 40 values of the power input P_{net} ranging from 0 to 9 MW, with the electrolyzers considered degraded and not degraded with the degradation profiles investigated in. ^{13,21} Figure 5 shows the optimal values for the relevant controller setpoints \mathbf{u} , as well as the HTO and the electrolyzer temperatures T^{El} for the undegraded case.

These two controlled variables determine the operational limits of the plant. When they can no longer be controlled to their maximal setpoints, the plant must either shut down (lower limit) or power must be discarded (upper limit). Both limits are shown in Figure 5 as red boxed regions. In the undegraded case there are three operating regions enclosed by these operating limits:

1. In the first operable region from $0.85 \,\mathrm{MW}$ to $1.84 \,\mathrm{MW}$ the HTO is at its upper

constraint and must therefore be controlled. The pressure and the lye recirculation rates can be used to do so, and both should increase with rising power as the cross-contamination becomes relatively less important.

- 2. Starting from 1.84 MW the current density in the electrolyzer is high enough to allow for both the lye flow rate and the pressure to assume their upper bounds. The temperature continues to rise with increasing power in this region without cooling having to be applied.
- 3. At input powers above 5.3 MW the electrolyzers reach their maximal temperature of 80 °C, from which point on the cooling water flow needs to gradually increase. At input powers of 6.83 MW the system cannot be sufficiently cooled anymore, i.e., the maximum allowable power input is reached.

In case some of the electrolyzers are degraded, the upper temperature limit is reached at lower power inputs, giving rise to an additional operating region:

4. In case of differing thermal characteristics of the stacks, the lye flow rates to the degraded electrolyzers should be reduced to maintain equally high temperatures amongst all stacks.

A thorough discussion on this last operation region can be found in Rizwan $et\ al.$, Cammann $et\ al.$.

4.2.2 Optimal operation

Low-load regions: HTO control At low loads the HTO can be controlled by manipulating both the lye recirculation rate and the system pressure. The losses incurred by suboptimal operation in this region are generally low, and we therefore propose a pragmatic and robust control approach. We do so by adopting a Split-Parallel Control (SPC) architecture, 28,29 consisting of two concentration control structures with different setpoints that act on the separator pressure and the lye flow rate controllers, respectively. The HTO setpoints are

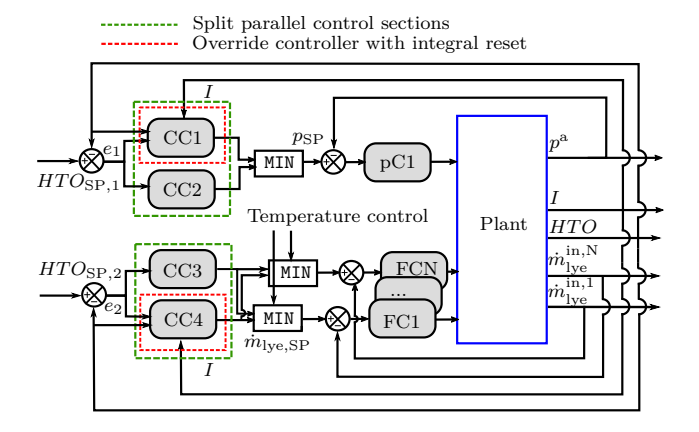


Figure 6: Control logic for using the pressure and the lye flow rates to control the *HTO*. The architecture is divided into two Split-Parallel Control sections, each with one fast-acting controller (CC2 or CC3) and one constraint-tracking controller with integral reset (CC1 and CC4).

below the alarm limit of 2% and ordered by the priority according to which nominal setpoint should be given up first. We chose to give up the lye flow rate setpoints first, as they are further from their upper bound for most of the low-load region and are associated with a smaller relative control effort. Both parts of the Split-Parallel Control structure have an override logic as presented in Sec. 3.1, using one fast-acting concentration controller to reject unmeasured disturbances and one slower override controller with integral reset. The integral reset is triggered every time a low-load region is approached:

$$t_{\rm r}(t) = \max\{t_{\rm i} \le t | I^{\rm k} \le 800 \& dI^{\rm k} \le -1 \ \forall k \in \mathcal{K}\}.$$
(11)

Here, $I^{\rm k}$ is the current density of stack k in A m⁻² and $dI^{\rm k}$ is its respective derivative with respect to time. Together with the integral reset controllers, there are in total four concentration controllers, of which all are master controllers to their respective slave control loops and have saturation blocks that limit the output within a certain range. Figure 6 shows a functional overview of the proposed overall HTO control logic; a comparative discussion of its step response with and without the integral reset can be found in Sec. 5.2.1.

High load regions: Temperature control We propose the temperature control logic shown in Figure 7 which is modeled after the

"hierarchical override with input resetting" presented in Sec. 3.2. The shared utility with the highest gain for the stack temperatures is the cooling water flow rate manipulated by TC4, which receives the highest measured stack temperature as selected by a MAX-selector. Setting the setpoint of TC4 to the maximal temperature $T_{\rm SP} = 80\,^{\circ}{\rm C}$ enforces that the cooling water flow rate is at its lower bound as long as the limiting temperature is not reached. As the cooling water flow rate is then determined by the electrolyzer which is most thermally constrained, temperatures in the other stacks are reduced if their flow rates are kept unchanged. Therefore, additional temperature controllers TC1-TC3 facilitate flow rate adjustments. Their setpoints are the lowest value between $T_{\rm SP}$ and the highest measured and filtered (first-order, $\tau = 50 \,\mathrm{s}$) stack temperature, considering a deadband between 0 and 348 K. These latter steps are done to ensure that the lve flow rates are only reduced for temperature control if a) one of the stack temperatures is near or above its setpoint, and b), if this elevated temperature is sustained for a sufficiently long time.

Note that the outputs of the temperature controllers TC1-TC3 are flow rate setpoints, which can be overridden by the *HTO* control through MIN-selectors, as shown in Figure 7.

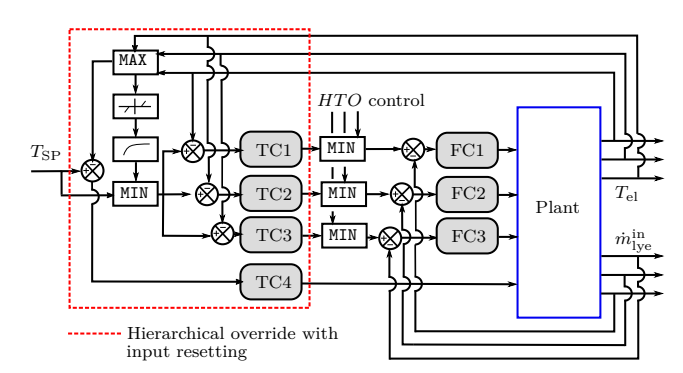


Figure 7: Logic for the overall temperature control structure. TC4 acts on the cooling water flow rate, whereas TC1-TC3 manipulate lye flow rate setpoints that can be overriden by the HTO control loop.

Production rate and inventory control For the considered process, the throughput is mainly determined by the applied power and, hence, the applied gas production rate in the electrolysis stacks. For consistency of the inventory system, it is required that the inventory "radiates" from the main throughput manipulator, i.e., that it is in the direction of flow downstream of it. For the gas-liquid separators, this results in a classical process control approach with the pressure being manipulated by the gas outflow, whereas the liquid level is controlled by the liquid outflow valve. Accordingly, the pressure of the storage tank is controlled by its outflow valve. As the purpose of the storage tank is to allow for independent operation of the electrolysis system while satisfying a constant demand, its pressure is left floating with two pressure controllers overriding the demand flow controller in case the high or low pressure setpoint, respectively, is reached. In the interest of space, this logic is shown only in the overview Figure 8.

4.2.3 Interconnections, overview, and numerical implementation

Figure 8 shows the developed control structure, in which the control signals related to the temperature control loops are highlighted in red, whereas those pertaining to the HTO and inventory control loops are shown in green and blue, respectively. All controllers are tuned as PI controllers using SIMC tuning rules²⁵ based on input step responses. To achieve both good performance and robustness, controllers are tuned by choosing the closed-loop time constant according to established recommendations. Special care is taken to match the time constants for the pressure difference control loop, and the temperature controller and the integral reset controllers CC1 and CC4 are tuned to achieve overdamped closed-loop behavior. App. C reports the tuning procedure in greater detail.

All simulations are conducted using the Julia programming language (v.1.11.2). The optimal scheduling problem in Eq. 8 is solved using the Gurobi solver with standard settings; the steady-state optimization problem in Eq. 9 is solved using IPOPT, ³⁰ also with standard set-

tings. Both optimizers are interfaced through the JuMP package (v. 1.23.5).³¹ Control simulations are done using the ModelingToolkit package (v. 8.71.1)³² using the Rodas5P solver with absolute and relative tolerances of 10^{-10} and 10^{-12} , respectively.

5 Results

We present a simulation case study to answer our posed research questions. The purpose of this case study is to verify the applicability of the proposed ARC structure and to compare it to relevant alternatives. To this end, the main points of comparison are the operating limits, dynamic efficiency, robustness to disturbances, and potential cost savings.

5.1 Overview of considered control structures

Often in industrial practice suboptimal operation is tolerated for the ease of constant setpoint operation. We therefore compare our proposed control structure (ARC) to three regulatory control structures with fixed setpoints (R1-R3) and to a regulatory control structure receiving hourly setpoint updates from an optimization layer (RTO). This difference is illustrated in Figure 9 for the case of the pressure control of the anodic separator pressure. A comparison of the relevant setpoints for the control structures is shown in Table 2, which also reports the load ranges obtained by solving the steady-state optimization problem in accordance to Eq. 9.

Table 2: Overview of the setpoint ranges for the considered control structures. The ranges for the applied power P depend on whether the electrolyzers are degraded (deg.) or not.

	$p_{\rm a}$ [bar]	\dot{m}_{lye} [kg s ⁻¹]	P [MW]	P (deg.) [MW]
ARC/RTO	7.5 - 15	1 - 10	0.85 - 6.83	1.28 - 5.97
R1	15	10	1.81 - 6.83	1.92 - 5.76
R2	7.5	1	0.85 - 5.87	1.39 - 4.24
R3	7.5	10	1.07 - 6.61	1.28 - 5.76

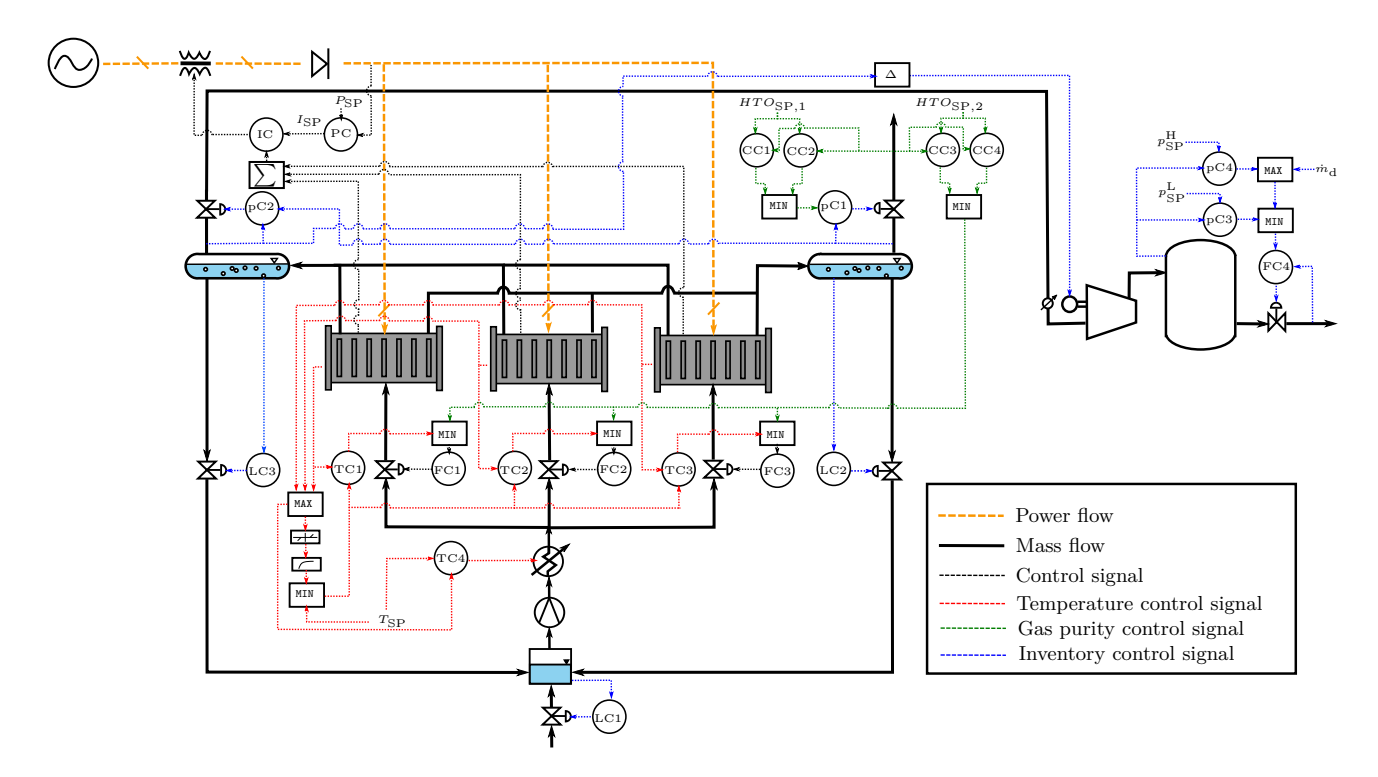


Figure 8: Overview of the developed advanced regulatory control structure. Control signals pertaining to the temperature control loops are shown in red, those related to the gas purity and inventory control loops in green and blue, respectively.

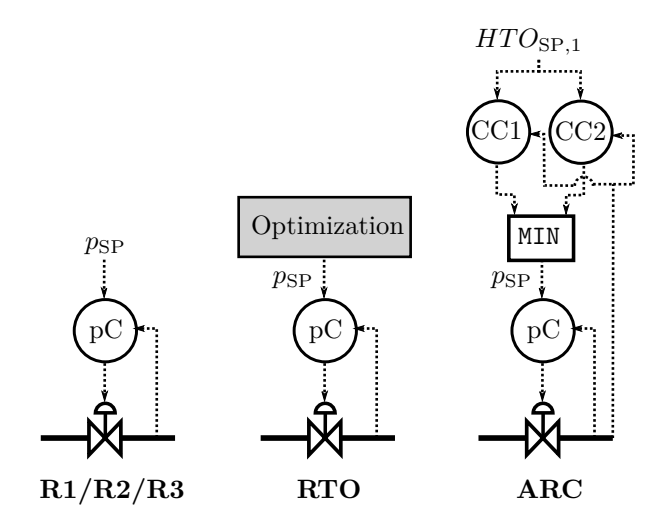


Figure 9: Example of different control strategies illustrated with the anodic separator pressure. Purely regulatory control (R1, R2, R3) receives constant setpoints, whereas setpoints follow from an optimization layer in the RTO case and from advanced selector logic in the ARC case.

Control structure R1 has constant high pressure and high lye flow rate setpoints. This increases the efficiency but comes at the expense of an increased minimum load (1.81 MW). Contrary to that, R2 has low pressure and low lye flow rate setpoints. This reduces the minimum load (0.85 MW), but also the efficiency and the cooling capacity at high loads. R3 is a compromise, where the pressure is kept low but the lye flow rate is kept high. Finally, ARC and RTO both facilitate flexible operation, thereby extending the load range and increasing the efficiency. As the setpoint ranges for both are the same, their steady-state operating limits are as well. These operating limits are broader than those of all considered regulatory control structures.

5.2 Control simulations

We first present step responses of the safety-relevant HTO control structure before simulating one day of operation with historical electricity prices. This includes scheduled power changes and an unmeasured disturbance to as-

sess efficiency and robustness across all control structures.

5.2.1 Process safety during power ramp downs

Figure 10 shows simulation results of the gas purity to the ramping sequence $P_{\text{max}} \xrightarrow{3h} P_{\text{min}} \xrightarrow{5h} 3\,\text{MW}$ with the HTO control structure with and without the integral reset. In the former case, the response to the ramping sequence is governed by the controllers CC1 and CC4 (shown in blue), in the latter, by CC2 and CC3 (shown in green).

Using the integral reset leads to an overshootfree response in the HTO. Without the integral reset, the HTO settles faster but overshoots the desired setpoint by 0.03 percentage points (relative overshoot 2%). As alluded to before, the second major benefit of employing the integral reset is that the setpoint is approached from the most conservative operating point. This becomes clear when considering the second panel in Figure 10 which shows the unmeasured values for the gas composition entering the gasliquid separator ($HTO^{\text{in}} = \dot{n}_{\text{H}_2}^{\text{out},a}/\dot{n}_{\text{O}_2}^{\text{out},a}$): Not employing the integral reset causes the composition in the incoming stream to exceed the highest setpoint $HTO_{SP,1}$ for 13 min, and even reach values that would trigger the alarm limit (AL) if they could be measured. With the integral reset, the unmeasured composition into the gas-liquid separator only briefly exceeds $HTO_{SP,1}$ and stays far from the alarm limit. The reason for this can be seen in the lowermost panel of Figure 10, which shows the outputs of the involved controllers. Considering integral reset, the controllers CC1 and CC4 reduce the output to their respective minimum bound shortly after the power drop at 3 h when the condition on the current density (Eq. 6) is satisfied. The lye flow rate stays at its lower bound, while the pressure increases to control the HTO to its higher setpoint. In contrast, without the integral reset, the controllers CC2 and CC3 only reduce their output once their respective setpoints are breached, which takes 20 min in the case of CC2 for pressure manipulation.

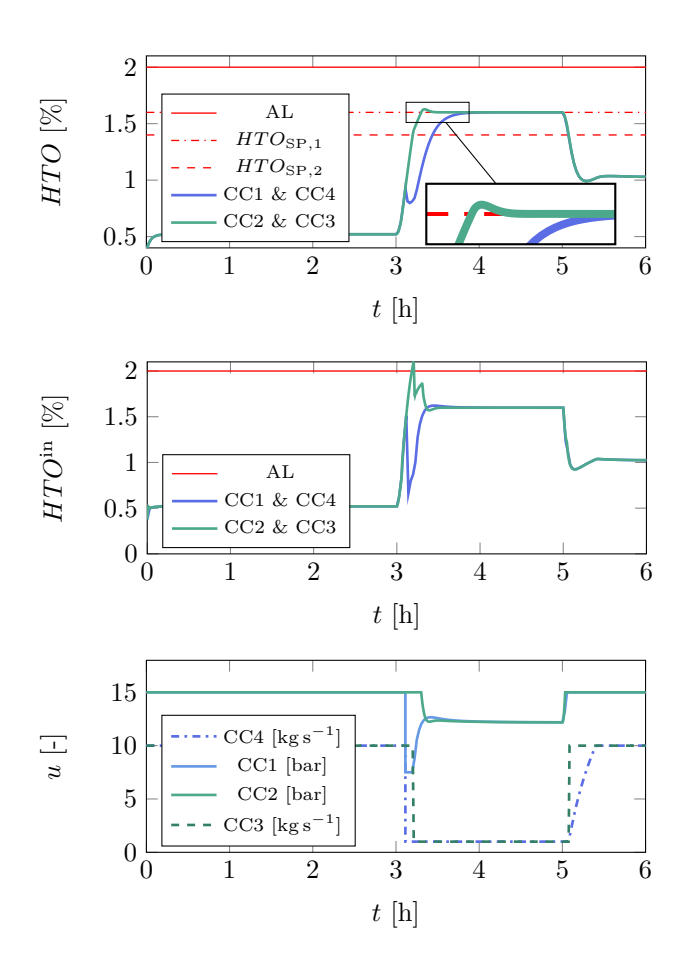


Figure 10: HTO and incoming HTO (upper two panels) and controller outputs for a scheduled power sequence with, and without the integral reset controllers. The former is shown in blue and the latter in green.

We note that in either case the alarm limit on the HTO measurement is not breached. While this limit of 2\% gives a large backoff to the lower explosion limit of 4\%, we nonetheless deem it desirable to be conservative also for gas compositions at locations without direct measurements. During the ramp from $P_{\text{max}} \rightarrow P_{\text{min}}$ the overshoot in the measurement without the integral reset controller is small, while the overshoot in the incoming gas composition is high. We found that ramping from lower powers without the integral reset yields the opposite effect, i.e., higher overshoots in the measurement and lower overshoots in the unmeasured incoming composition. This is because at lower powers the initial HTO is higher and the setpoints of the concentration controllers are reached faster.

5.2.2 Operation with ARC

Figure 11 summarizes the main process variables for the degraded system with ARC during a challenging day of a typical operation week, characterized by frequent power changes. The scheduled power profile is obtained from the weekly optimization described in the next The system tracks power setpoints well, including transitions to and from the minimum and maximum load. The stack temperatures generally increase or decrease with the applied power, without greatly exceeding the upper bound of 80 °C. The highest overshoot in the temperature is found to be 1.43 °C when ramping up to P_{max} . As the stacks have differing thermal characteristics, the steady-state temperature differs during times when minimal cooling water is supplied, i.e., at low powers. When cooling must be applied at high powers, e.g., in the hours 1 and 2, the lye flow rates into the individual electrolyzers is automatically adjusted to facilitate equally high temperatures. The HTO shows an opposite trend, rising at low power and falling during periods of elevated power. The integral reset controllers CC1 and CC4 ensure that the HTO setpoint is smoothly approached from below during low power periods. The effect of the integral reset can be seen, e.g., in the pressure, which rapidly reduces in power downturns before increasing again for safe control.

Overshoots in the HTO can occur during periods with unmeasured disturbances (marked by orange lines in the relevant plots). Here, an increase in gas crossover in the electrolyzers occurs ($\dot{n}_{\rm H_2,conv}=0.01\,{\rm mol\,s^{-1}}$) that is not related to the applied power and could be caused by, e.g., a mechanical fault. Control action is only taken as soon as the respective HTO setpoint is breached from below, here by 0.085%. For this disturbance, only $HTO_{\rm SP,2}$ is exceeded, prompting the fast-acting CC3 controller to reduce the lye flow rate and stabilize the HTO before the pressure-acting concentration controller has to act.

Among the manipulated variables, lye flow rates exhibit the greatest variability, as they serve both temperature and HTO control. At

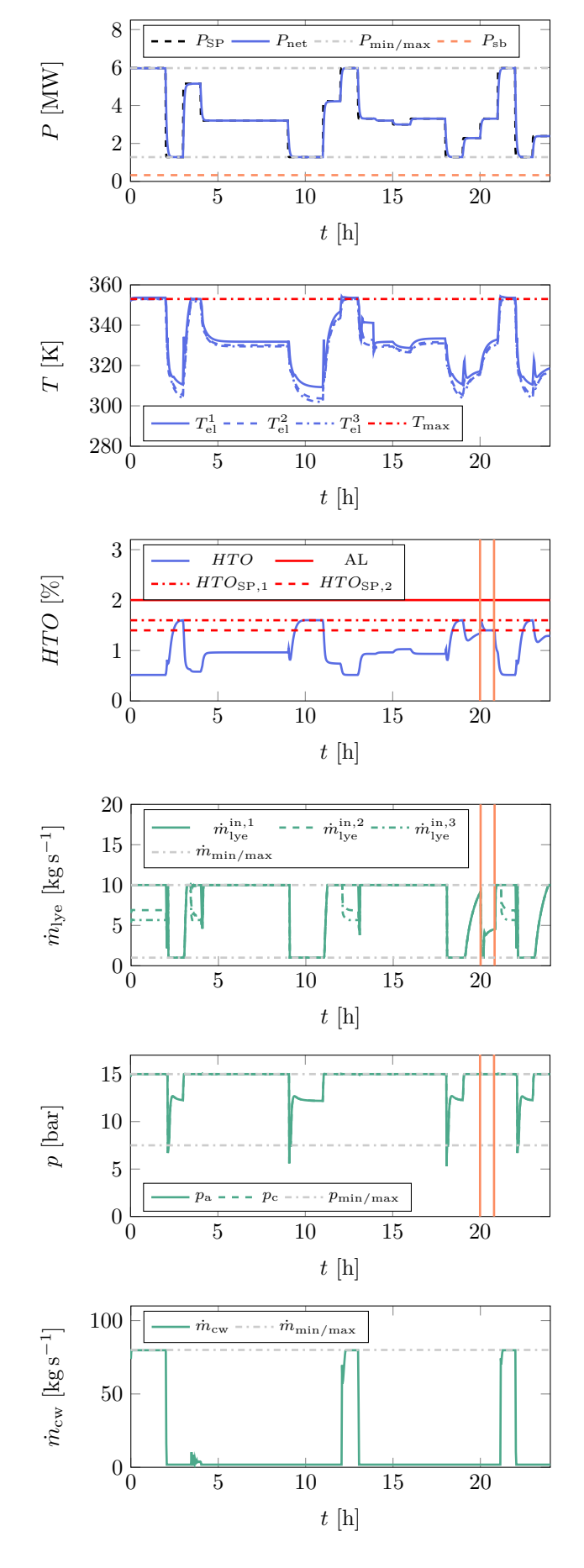


Figure 11: Overview of the most important process variables on day 5 using the ARC structure.

14 Vertical orange lines highlight the time during which an additional disturbance is applied.

low loads, concentration control dominates, leading to uniform flow rates across the stacks; at high loads, temperature control dominates, causing divergence between the stacks. The pressure and the cooling water flow rate adjust less frequently and as expected, with the former reduced during low-load operation by the integral reset and cooling activated only at high power levels. The pressure difference control ensures that the anode and cathode side pressures are almost identical, with the biggest pressure difference being half of the allowable value (Eq. 2j).

5.3 Comparison with other control structures

We compare ARC to an RTO implementation and regulatory control layers (R1-R3) under the previous power schedule that was optimized for flexibly operating plants. The RTO layer provides hourly setpoint updates based on the steady-state optimization problem given the respective scheduled power. In the RTO layer the cooling water flow rate $\dot{m}_{\rm cw}$ is not explicitly supplied to prevent unnecessary cooling during transients; instead, it is set by TC4.

Table 3: Maximal gas impurity HTO^* , maximal temperature $T_{\rm el}^*$ and average efficiency $\overline{\eta}_{\rm d}$ with different control structures with the same simulated power schedule.

		RTO	ARC	R1	R2	R3
$\begin{array}{c} HTO^* \\ T_{\rm el}^* \\ \overline{\eta}_{\rm d} \end{array}$	[%]	1.92	1.6	2.48	1.14	1.25
	[K]	356.1	354.3	355.4	385.4	354.7
	[kWh/kg]	48.9	49.04	49	49.44	49.45

Table 3 shows the highest measured gas impurity HTO^* and stack temperature $T_{\rm el}^*$, as well as the daily average system efficiency $\overline{\eta}_{\rm d}$ for all control structures. As expected, the RTO implementation achieves the best efficiency value with 48.9 kWh/kg. However, it is not robust towards the unmeasured gas-crossover disturbance, exceeding the upper HTO setpoint by 0.32% (relative overshoot 20%). On the other hand, our proposed ARC structure shows no significant overshoot even under disturbed operation. Its efficiency is 0.29% lower than the

RTO implementation, while R2 and R3 exhibit higher efficiency losses ($\approx 1.1\%$). R1, with constant high pressure and lye flow rate setpoints, is slightly more efficient than ARC but exhibits the highest gas-impurity peak of 2.48%.

5.4 Operation over a typical week

We now consider the daily power dispatch profile obtained by solving Eq. 12 sequentially for the timespan of one week. The inputs include the wholesale electricity prices of the NO3 region in Norway (18. Nov. 2024 to 25. Nov. 2024, Figure 12a), 33 the production curve, as well as operating constraints P_{\min} to P_{\max} . Since these figures depend on the pressure and lye recirculation, we compare weekly costs for flexible (ARC, RTO) and fixed-setpoint strategies (R1-R3). The relevant operating ranges are summarized in Table 2, the production efficiency curve is parametrized for each configuration and reported in App. A.

Figure 12b shows the optimal power dispatch for a flexible control structure under degraded conditions. The optimal power profile follows the price signal, operating at high powers during low prices and standby during peaks. Overall, intermediate powers are less common, suggesting that tighter operating constraints will reduce the economic performance. This is indeed the case, as can be seen in Table 4, where the electricity cost $J_{\rm cost}$ and average efficiency for this week $\overline{\eta}_{\rm w}$ are summarized for each control configuration both in the degraded and the non-degraded case. Flexible operation yields

Table 4: Comparison of control structures under degraded and undegraded plant states.

	$\overline{\eta}_{ m w} \ [{ m kWh/kg}]$	J_{cost} $[\in]$	$\overline{\eta}_{ m w}~({ m deg.}) \ [{ m kWh/kg}]$	J_{cost} (deg.) $[\in]$
ARC/RTO	50.2	9012.7	50.7	9498.7
R1	50.5	9341.4	51.4	9742.3
R2	49.6	9317.9	51.8	9964
R3	50.8	9436.1	50.1	9557

the lowest costs for both cases, being 9013€ and 9499€, respectively. R2 ranks second in the undegraded case but worst in the degraded case

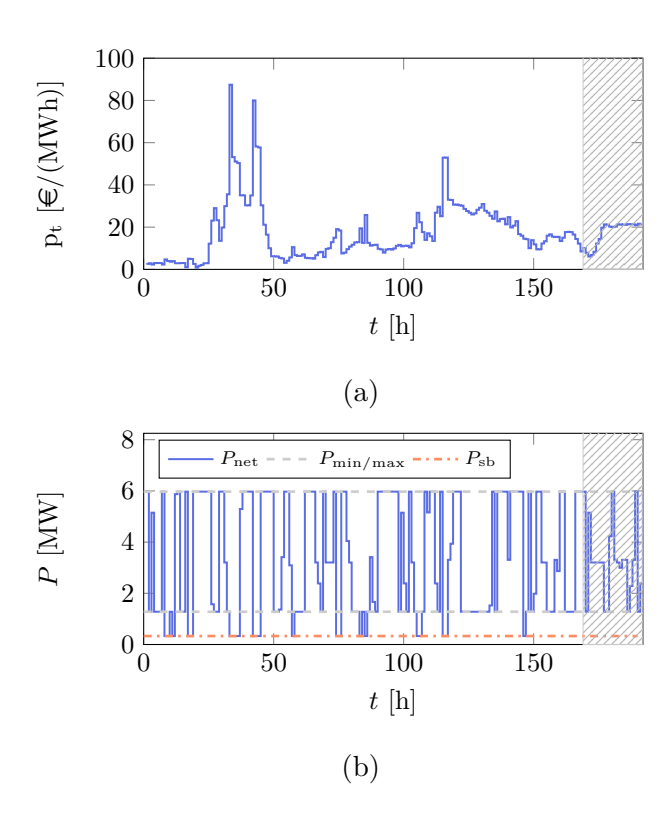


Figure 12: Electricity prices considered in this study (a), and resulting optimally scheduled powers for the timespan (b). Greyed-out areas are those considered for the detailed 24 h simulation.

due to its strongly reduced upper load limit. Cost savings afforded by flexible operation relative to the next best option amount to 58€ in the degraded case and 305€ in the undegraded case. It is worth noting that the weekly averaged efficiency for the flexible operation is only the second best among the considered options. This further corroborates the idea that extending the operating limit is important for economically efficient operation in the day-ahead electricity market. Evidently, good efficiency values do not lead automatically to economically optimal performance if the operating window of the plant is strongly constrained.

6 Discussion

We present the discussion section in two parts. Each part addresses one of the outlined research questions considering the presented results and discusses the findings in a broader context.

6.1 Q.1: Implementation of flexible operation using simple elements and comparison with alternatives

Our proposed ARC control structure enables flexible operation by using simple control elements to switch between relevant operating regions. We addressed the key challenge of extending the lower and upper load limits by introducing two advanced regulatory elements: Override control with integral reset and hierarchical override with input resetting.

A key advantage of our approach is that optimal operation is embedded directly in the regulatory control layer, reducing reliance on model-based strategies like RTO. This is beneficial since developing and maintaining accurate models, especially for large plants and safetycritical variables like the HTO, is costly and demanding. Optimal curve tracking methods, such as those in Hu et al. and Li et al., depend on high-fidelity models and are thus sensitive to modeling errors and disturbances. Our case study illustrates this: while RTO achieved the highest efficiency, it failed to prevent excessive HTO increases under unmeasured disturbances. In the considered N-in-1 configuration with two degraded electrolyzers, the optimal curve shifts, and plant-model mismatch would exacerbate deviations. In contrast, our ARC structure performed reliably even when tuned on the undegraded system. This fundamental advantage is afforded by the integral reset control, which is designed to approach the HTO setpoint from the most conservative operating region.

An alternative we have not explored is economic MPC, which could offer robust performance at the cost of increased modeling effort and reduced operator interpretability. Given that safety-critical variables like *HTO* require extensive regulatory logic (e.g., for automatic shutdowns), we argue that designing this logic a priori to support near-optimal operation is preferable—especially in grid-coupled electrolysis, where longer settling times allow for steady-state optimization.

6.2 Benefit of flexible operation for participation in the day-ahead electricity market

Increasing the operational flexibility of water electrolysis plants offers several advantages. As shown in Table 2, smart manipulation of process variables can extend the load limits by up to 50% in extreme cases compared to fixed setpoint operation. This relaxation of operating constraints can considerably reduce operating costs, with our analysis showing savings of up to 4.9% during a typical week in November 2024. Additionally, flexible operation improves efficiency relative to most conventional regulatory structures.

While we excluded participation in the power reserve market, prior studies indicate that it can enhance the profitability of alkaline water electrolyzers³⁴ and that understanding process dynamics helps relax bidding constraints.³⁵ For sudden, unscheduled frequency reserve provision, our override control with integral reset could offer dynamic safety buffering. Moreover, the ARC structure supports safe operation in high time-resolution electricity markets, though under these conditions steady-state might no longer be guaranteed during each time window. Such requirements would then need to be embedded in the scheduling layer.

7 Conclusion

This paper is concerned with the flexible operation of pressurized, strongly coupled alkaline water electrolyzers in the day-ahead electricity market. To this end, we have developed a detailed dynamic model of the process as well as an advanced regulatory control structure for it. This control structure requires only standard control elements to switch between relevant operating regions. At its heart lie two advanced regulatory control elements, which we have developed to ensure satisfaction of gas purity and temperature constraints.

We estimated the economic potential of flexible operation by solving an optimal power dispatch problem over one week using historical electricity prices. Depending on the system degradation and pressure level, cost reductions ranged from 0.6% to 3.5% compared to fixed-setpoint operation. Dynamic simulations for a representative day demonstrated that our control structure gives essentially perfect control of the safety-critical HTO even with degradation not accounted for in the controller tuning and outperforms both RTO-based and conventional regulatory control in disturbance rejection. While RTO achieved slightly higher efficiency, our approach showed only a 0.2% reduction and offered superior robustness.

Given its simplicity and interpretability, the proposed control scheme warrants experimental validation on physical systems and could be adapted to proton-exchange membrane electrolyzers. Although designed with grid dynamics in mind, its applicability to directly coupled renewable operation should be further investigated. A direct comparison with economic MPC under varying power profiles would also be valuable.

Nomenclature

Abbreviations

AEL Alkaline electrolysis

AL Alarm limit

ARC Advanced regulatory control

BoP Balance of plant

DMC Dynamic matrix control

DOF Degree of freedom

FC Flow controller

HTO Hydrogen-to-oxygen

IC Current controller

IPOPT Interior point optimizer

LC Level controller

MPC Model predictive control

nMPC Nonlinear model predictive control

OCT	Optimal curve tracking	J	Cost term (\leqslant)
ОТН	Oxygen-to-hydrogen	$K_{\rm p}$	Proportional gain (Variable unit)
PC	Power controller	l	Liquid level (m)
pC	Pressure controller	\dot{m}	Flow rate $(kg s^{-1})$
PΙ	Proportional-Integral	$\dot{m}_{ m d}$	Hydrogen demand $(kg h^{-1})$
PID	Proportional-Integral-Derivative	M	$Molar mass (g mol^{-1})$
R	Regulatory control	m	Mass inventory (kg)
RTO	Real-time optimization	\dot{n}	Flow rate $(kg s^{-1})$
SPC	Split-Parallel Control	n	Molar inventory (mol)
TC	Temperature controller	$n_{\rm c}$	Number of cells (-)
Symb	ools	p	Price (variable unit)
A	Area (m^2)	\overline{P}	Upper segment power (W)
$B_{\rm c}$	Segment slope $(kg h^{-1} MW^{-1})$	<u>P</u>	Lower segment power (W)
c	Concentration (mol m^{-3})	P	Power (W)
$C_{\rm c}$	Segment intercept $(kg h^{-1})$	p	Pressure (bar)
$C_{\rm p}$	Heat capacity $(J kg^{-1} K^{-1})$	$P_{\rm net}$	Total power (W)
$C_{ m t}$	Stack thermal capacity (joule/kg)	R	Universal gas constant $(J \operatorname{mol}^{-1} K^{-1})$
D	Diffusion coefficient $(m^2 s^{-1})$	r	Reference signal (variable unit)
d	Disturbance signal (variable unit)	S	Solubility constant $(\text{mol kg}^{-1} \text{bar}^{-1})$
$d_{\rm e}$	Flow height (m)	$ ilde{T}$	Mixing temperature (K)
$d_{ m m}$	Membrane thickness (m)	T	Temperature (K)
e	Error signal (-)	t	Time (s)
F	Faraday constant $(C \text{ mol}^{-1})$	$T_{ m i}$	Integral time constant (K)
f()	Differential equation	U	Voltage (V)
G	Transfer function (variable unit)	u	Input signal (-)
g()	Algebraic equation	UHX	Heat exchanger capacity (W K^{-1})
h()	Inequality constraint	V	Volume (m ³)
$h_{\rm c}$	Convective heat transfer coefficient	x	Mole fraction (-)
7	$(W m^{-2} K^{-1})$	${f z}$	Electrolyzer state (-)
I	Current density $(A m^{-2})$		

y	Measurement signal (-)	cs	Cold side
z	Electron transfer number (-)	ctr	Control signal
$z_{ m i}$	Valve opening i (-)	cw	Cooling water
β	Setpoint weight (-)	diff	Diffusive
ϵ	Emissivity constant (-)	el	Electrolyzer
η	Production efficiency (kWh/kg)	F	Faradic
$\eta^{ m k}$	Overvoltage (volt)	f	Flow
γ	Heat capacity ratio (-)	g	Gas
κ	Conductivity $(S m^{-1})$	HEX	Heat exchanger
λ	Generic efficiency (variable unit)	hs	Hot side
$\mathcal J$	Set of species	in	Incoming to unit
\mathcal{K}	Set of electrolyzers	k	Electrolyzer index
$\mathcal S$	Set of compartments	1	Lye
\mathcal{T}	Set of hours	\log	Logarithmic
$\overline{\eta}$	Average production efficiency (kWh/kg)	m	Membrane
ρ	Density $(kg m^{-3})$	max	Maximum value
σ	Stephan-Boltzmann constant (W $\rm m^{-2}K^{-4})$	min	Minimum value
au	Time constant (s)	out	Outgoing of unit
$ au_{ m c}$	Closed loop time constant (s)	prod	Production
θ	Bubble coverage (-)	prof	Profit
$ heta_{ m d}$	Time delay (s)	r	Reactive
Subs	${ m cripts/Superscripts}$	rev	Reversible
a	Anode	ru	Ramp-up status
a	Ambient	s	Side index (Anode/Cathode)
bf	Buffer	off	Off status
c	Segment index	on	On status
co	Compressor	S	Surface
conv	Convective	sb	Standby status
cost	Electricity cost	sep	Separator

SP Setpoint

sto Storage

T Tracking

t Time index

w Week

j Species index

* Highest value

0 Reference

A Scheduling layer

Typically, settled electricity prices are revealed one day in advance at gate-closing time. Plant operators can then procure power on an hourly basis. To meet the designated daily production target under minimal electricity costs, the following optimization problem in Eq. 12 is solved. When solving the problem consecutively for one week (Sec. 5.4) the initial gas storage level m_1^{sto} is taken as the last storage level of the previous day.

A.1 Optimization problem

The full optimization problem referred to in Section 4.1 is mainly inspired by Raheli *et al.* and written out as follows:

$$\min_{\mathbf{z},\mathbf{P}} \sum_{\mathbf{t} \in \mathcal{T}} \mathbf{p}_{\mathbf{t}} P_{\text{net},\mathbf{t}} + \mathbf{p}_{\text{ru}} \mathbf{z}_{\mathbf{t}}^{\text{ru}} - \dot{m}_{\mathbf{t}}^{\text{prod}} \mathbf{p}_{\mathbf{H}_{2}} \tag{12}$$

$$\mathbf{s.t.0} = m_{\mathbf{t}}^{\text{sto}} - m_{\mathbf{t-1}}^{\text{sto}} + \dot{m}_{\mathbf{d}} - \dot{m}_{\mathbf{t}}^{\text{prod}} \qquad \forall t \in \mathcal{T}/\{1\},$$

$$0 = \mathbf{z}_{\mathbf{t}}^{\text{on}} + \mathbf{z}_{\mathbf{t}}^{\text{sb}} + \mathbf{z}_{\mathbf{t}}^{\text{off}} - 1 \qquad \forall t \in \mathcal{T},$$

$$0 = P_{\text{net},\mathbf{t}} - \mathbf{z}_{\mathbf{t}}^{\text{sb}} P_{\text{sb}} - \sum_{c \in \mathcal{C}} \hat{P}_{c,\mathbf{t}} \qquad \forall t \in \mathcal{T},$$

$$0 = \dot{m}_{\mathbf{t}}^{\text{prod}} - \sum_{c \in \mathcal{C}} (B_{c} \hat{P}_{c,\mathbf{t}} + C_{c} z_{c,\mathbf{t}}) \qquad \forall t \in \mathcal{T},$$

$$0 = \mathbf{z}_{\mathbf{t}}^{\text{on}} - \sum_{c \in \mathcal{C}} \mathbf{z}_{c,\mathbf{t}} \qquad \forall t \in \mathcal{T},$$

$$\mathbf{z}_{\mathbf{t}}^{\text{on}} + \mathbf{z}_{\mathbf{t}}^{\text{sb}} + \mathbf{z}_{\mathbf{t-1}}^{\text{off}} - 1 \leq z_{\mathbf{t}}^{\text{ru}} \qquad \forall t \in \mathcal{T}/\{1\},$$

$$\underline{P}_{c} z_{c,\mathbf{t}} \leq \hat{P}_{c,\mathbf{t}} \leq \overline{P}_{c} z_{c,\mathbf{t}} \qquad \forall t \in \mathcal{T}, c \in \mathcal{C},$$

$$z_{\mathbf{t}}^{\text{on}} P_{\text{min}} \leq P_{\text{net},\mathbf{t}} \leq P_{\text{max}} \qquad \forall t \in \mathcal{T},$$

$$m_{\text{sto,min}} \leq m_{\text{sto,t}} \leq m_{\text{sto,max}} \qquad \forall t \in \mathcal{T}.$$

Here, $m_{\rm t}^{\rm sto}$ is the mass of stored hydrogen at time t, $\dot{m}_{\rm d}$ and $\dot{m}_{\rm t}^{\rm prod}$ are then the constant

demand and the hydrogen produced, respectively. The latter is proportional to the applied $P_{\text{net.t}}$, and the so-called production curve relating both is fitted according to the stateof-the-art approximation using piecewise linearization. 26,36,37 This is further explained in Sec. A.2. The binary variable \mathbf{z}_{t}^{on} designates at which hours the electrolyzer is turned on, while $\mathbf{z}_{t}^{\text{sb}}$ and $\mathbf{z}_{t}^{\text{off}}$ designate hours during which the electrolyzer is in standby or off, respectively. Production can be instantly resumed from a standby state, during which 0.33 MW are consumed for stabilization, scaled from.³⁸ Offstates are undesirable as the following ramp-up **z**^{ru} incurs losses in terms of energy and time, which is accounted for in the objective with a penalty cost of $p_{ru} = 300 \in$, scaled from ^{26,27} to 6 MW. We assume a constant hydrogen price of $p_{\rm H_2} = 2.1$ e/kg²⁶ and a constant demand $\dot{m}_{\rm d}$ of $66.3 \,\mathrm{kg} \,\mathrm{h}^{-1}$, approximately the production using half of the nominal electrolyzer capacity with a constant efficiency of $\eta = 49 \,\mathrm{kWh/kg}$. Importantly, the power in the system must remain between the minimum power P_{\min} and the maximum power P_{max} in an operational state. Both of these values are informed by the steadystate model, and the task of the regulatory control layer is to facilitate safe and efficient operation between these bounds.

A.2 Production curves

To solve the scheduling problem for all control configurations, we fit each optimal steady-state production curve with a set of three line segments \mathcal{C} . In Eq. 12 the terms $B_{\rm c}$ and $C_{\rm c}$ refer to the respective slope and intercept of each line segment. ²⁶ The linearization points are found by identifying the three points for each production curve in which the rate of change of the slope is highest based on 65 discrete points between $P_{\rm min}$ and $P_{\rm max}$. In Eq. 12 the equality constraint

$$0 = \mathbf{z}_{t}^{\text{on}} - \sum_{c \in \mathcal{C}} \mathbf{z}_{c,t} \quad \forall t \in \mathcal{T},$$
 (13)

ensures that only one line segment is active at a time, indicated through the binary variable $\mathbf{z}_{c,t}$. Figure 13 shows the production curve and the corresponding fit on three line segments for the degraded system with flexible operation. Tables

5 and 6 present the fitted parameters for the considered control structures in the undegraded and degraded case, respectively. Note that the upper bound \overline{P}_c of each segment is the lower bound of the following segment \underline{P}_{c+1} , hence only the latter is shown. The upper bound of the last segment is equal to P_{max} for that configuration (see Tab. 2).

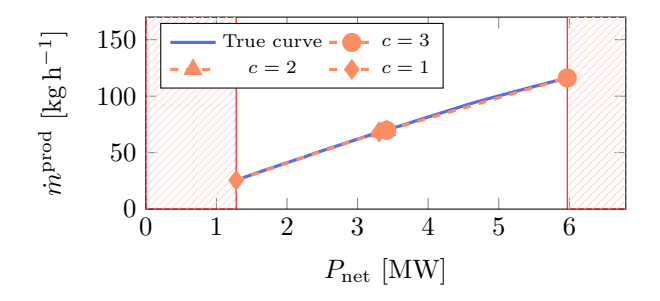


Figure 13: Production curve fit based on three line segments for the degraded plant with flexible operation. The feasible operating region is bounded by red boxes.

B Model parameters and derivations

The model parameters are presented in three tables. Parameters pertaining to the U-I curves of the electrolyzers are taken from 13 and 21 and summarized in Table 9. Sizing and design parameters are shown in Table 7, material and transport properties in Table 8.

B.1 Derivations

The pressure in the gas-liquid separators (Eq. 2a) is derived considering the ideal gas law:

$$\frac{\mathrm{d}p^s V_{\mathrm{g}}^s}{\mathrm{d}t} = \frac{\mathrm{d}(n_{\mathrm{g}}^s R \tilde{T})}{\mathrm{d}t},\tag{14}$$

$$\frac{\mathrm{d}p^s}{\mathrm{d}t}V_{\mathrm{g}}^s + \frac{\mathrm{d}V_{\mathrm{g}}^s}{\mathrm{d}t}p^s = R\tilde{T}\frac{\mathrm{d}n_{\mathrm{g}}^s}{\mathrm{d}t}.$$
 (15)

Here, $n_{\rm g}^s$ is the amounts of mole in the gas phase of the separator s while $V_{\rm g}^s$ its respective volume. The balance for the former is

$$\frac{\mathrm{d}n_{\mathrm{g}}^{s}}{\mathrm{d}t} = \sum_{k \in \mathcal{K}} \dot{n}_{\mathrm{j}}^{\mathrm{out},k,s} + \dot{n}_{\mathrm{i} \neq \mathrm{j,g}}^{\mathrm{in},s} - \dot{n}_{\mathrm{g}}^{\mathrm{out},s}$$

$$s, j = \{a, O_{2}\} \lor \{c, H_{2}\}$$
(16)

The first term denotes the main gaseous species entering the separator s, i.e., hydrogen at the anode side and oxygen at the cathode side. The second term is the amount of gas not dissolved in the liquid according to Henry's law (Eq. 2g) while the last term is the amount of gas over the gas outlet valve. The derivative of the gas volume is found considering that the constant volume in the separator is occupied by the gas and liquid phase volume (Eq. 2e):

$$\frac{\mathrm{d}V_{\mathrm{g}}^{s}}{\mathrm{d}t} = -\frac{\mathrm{d}V_{\mathrm{l}}^{s}}{\mathrm{d}t} = -(0.5\sum_{k \in \mathcal{K}} \dot{m}_{\mathrm{lye}}^{\mathrm{out},k} - \dot{m}^{\mathrm{out},s})/\rho_{\mathrm{l}} \quad (17)$$

Upon insertion of Eq. 16 and Eq. 17 in Eq. 15, the Eq. 2a is found. The molar component balance in the gas phase is similarly derived:

$$\frac{\mathrm{d}n_{\mathrm{g},j}^{s}}{\mathrm{d}t} = \frac{\mathrm{d}x_{j}^{s}n_{\mathrm{g}}^{s}}{\mathrm{d}t} = \dot{n}_{\mathrm{j}}^{\mathrm{in},s} - x_{j}^{s}\dot{n}_{\mathrm{g}}^{\mathrm{out},s}$$
(18)

$$\frac{\mathrm{d}n_j^s}{\mathrm{d}t} = \frac{\mathrm{d}x_j^s}{\mathrm{d}t} \frac{p^s V_\mathrm{g}^s}{R\tilde{T}} + \frac{\mathrm{d}n_\mathrm{g}^s}{\mathrm{d}t} x_j^s \tag{19}$$

$$\leftrightarrow \frac{\mathrm{d}x_{j}^{s}}{\mathrm{d}t} = \frac{R\tilde{T}}{p^{s}V_{\mathrm{g}}^{s}} \left(\dot{n}_{j}^{\mathrm{in},s} - x_{j}^{s} \dot{n}_{\mathrm{g}}^{\mathrm{out},s} - x_{j}^{s} \dot{n}_{\mathrm{g}}^{\mathrm{out},s} \right) - x_{j}^{s} \left(\dot{n}_{j}^{\mathrm{in},s} + \dot{n}_{i}^{\mathrm{in},s} - \dot{n}_{\mathrm{g}}^{\mathrm{out},s} \right).$$
 (20)

Eq. 20 can be readily simplified by noting that the term $x_j^s \dot{n}_{\rm g}^{{\rm out},s}$ cancels out. Assuming that at elevated pressures and moderate temperatures the amount of water in the gas phase is negligible, we can use the closure relation $x_{\rm H_2}^s + x_{\rm O_2}^s = 1$ to express $\dot{n}_j^{{\rm in},s} = (x_{\rm H_2}^s + x_{\rm O_2}^s) \dot{n}_j^{{\rm in},s}$ and cancel further terms:

$$\frac{\mathrm{d}x_{j}^{s}}{\mathrm{d}t} = \frac{R\tilde{T}}{p^{s}V_{g}^{s}}(\dot{n}_{j}^{\mathrm{in},s}x_{i}^{s} + \dot{n}_{j}^{\mathrm{in},s}x_{j} - \dot{n}_{j}^{\mathrm{in},s}x_{j} - \dot{n}_{i}^{\mathrm{in},s}x_{j}),$$
(21)

$$=\frac{R\tilde{T}}{p^s V_{\sigma}^s} (\dot{n}_j^{\mathrm{in},s} x_i^s - \dot{n}_i^{\mathrm{in},s} x_j^s). \tag{22}$$

This is the equivalent to the form in Eq. 2c. We make similar use of the product rule to derive the equations for the liquid concentrations in the gas-liquid separator (Eq. 2d) and the buffer tank (Eq. 2d). Since they are constructed analogously, we present only the former:

$$\frac{\mathrm{d}n_{\mathrm{l},j}^{s}}{\mathrm{d}t} = \frac{\mathrm{d}c_{j}^{s}V_{\mathrm{l}}^{s}}{\mathrm{d}t} = \dot{n}_{\mathrm{l},j}^{\mathrm{in}} - \dot{m}^{\mathrm{out},s}c_{j}^{s}/\rho_{\mathrm{l}},\tag{23}$$

$$\frac{dn_{l,j}^{s}}{dt} = \frac{dc_{j}^{s}}{dt}V_{l}^{s} + \frac{dc_{j}^{s}}{dt}V_{l}^{s} = \dot{n}_{l,j}^{\text{in}} - \dot{m}^{\text{out},s}c_{j}^{s}/\rho_{l}, \quad (24)$$

$$\leftrightarrow \frac{\mathrm{d}c_j^s}{\mathrm{d}t} = \left(\dot{n}_{\mathrm{l},j}^{\mathrm{in}} - \dot{m}^{\mathrm{out},s}c_j^s/\rho_{\mathrm{l}} - c_j^s/\rho_{\mathrm{l}}(0.5\sum_{k \in \mathcal{K}} \dot{m}_{\mathrm{lye}}^{\mathrm{out},k} - \dot{m}^{\mathrm{out},s})\right)/V_{\mathrm{l}}^s.$$
(25)

Table 5: Overview of fitting parameters for production curve of different control structures in the undegraded case.

		Segments $c \in \mathcal{C}$	
	c = 1	c = 2	c = 3
ARC	$B_c = 23.1 \mathrm{kg} \mathrm{h}^{-1} \mathrm{MW}^{-1}$	$B_c = 20.99 \mathrm{kg} \mathrm{h}^{-1} \mathrm{MW}^{-1}$	$B_c = 20.38 \mathrm{kg} \mathrm{h}^{-1} \mathrm{MW}^{-1}$
	$C_c = -2.68 \mathrm{kg} \mathrm{h}^{-1}$	$C_c = 0.4 \mathrm{kg} \mathrm{h}^{-1}$	$C_c = 1.98 \mathrm{kg} \mathrm{h}^{-1}$
	$\underline{P}_c = 0.85 \mathrm{MW}$	$\underline{P}_c = 5.22 \mathrm{MW}$	$\underline{P}_c = 6.61 \mathrm{MW}$
R1	$B_c = 20.68 \mathrm{kg} \mathrm{h}^{-1} \mathrm{MW}^{-1}$	$B_c = 20.67 \mathrm{kg} \mathrm{h}^{-1} \mathrm{MW}^{-1}$	$B_c = 20 \mathrm{kg} \mathrm{h}^{-1} \mathrm{MW}^{-1}$
	$C_c = 1.65 \mathrm{kg} \mathrm{h}^{-1}$	$C_c = 1.68 \mathrm{kg} \mathrm{h}^{-1}$	$C_c = 3.82 \mathrm{kg} \mathrm{h}^{-1}$
	$\underline{P}_c = 1.81 \mathrm{MW}$	$\underline{P}_c = 5.33 \mathrm{MW}$	$\underline{P}_c = 6.61 \mathrm{MW}$
R2	$B_c = 20.92 \mathrm{kg} \mathrm{h}^{-1} \mathrm{MW}^{-1}$	$B_c = 20.89 \mathrm{kg} \mathrm{h}^{-1} \mathrm{MW}^{-1}$	$B_c = 20.86 \mathrm{kg} \mathrm{h}^{-1} \mathrm{MW}^{-1}$
	$C_c = 0.3 \mathrm{kg} \mathrm{h}^{-1}$	$C_c = 0.35 \mathrm{kg} \mathrm{h}^{-1}$	$C_c = 0.42 \mathrm{kg} \mathrm{h}^{-1}$
	$\underline{P}_c = 0.85 \mathrm{MW}$	$\underline{P}_c = 4.9 \mathrm{MW}$	$\underline{P}_c = 5.01 \mathrm{MW}$
R3	$B_c = 10.94 \mathrm{kg} \mathrm{h}^{-1} \mathrm{MW}^{-1}$	$B_c = 20.69 \mathrm{kg} \mathrm{h}^{-1} \mathrm{MW}^{-1}$	$B_c = 20.67 \mathrm{kg} \mathrm{h}^{-1} \mathrm{MW}^{-1}$
	$C_c = 10.26 \mathrm{kg} \mathrm{h}^{-1}$	$C_c = 0.911 \mathrm{kg} \mathrm{h}^{-1}$	$C_c = 0.28 \mathrm{kg} \mathrm{h}^{-1}$
	$\underline{P}_c = 1.06 \mathrm{MW}$	$\underline{P}_c = 5.22 \mathrm{MW}$	$\underline{P}_c = 5.33 \mathrm{MW}$

Table 6: Overview of fitting parameters for production curve of different control structures in the degraded case.

		Segments $c \in \mathcal{C}$	
	c = 1	c = 2	c = 3
ARC	$B_c = 21.04 \mathrm{kg} \mathrm{h}^{-1} \mathrm{MW}^{-1}$	$B_c = 21 \mathrm{kg} \mathrm{h}^{-1} \mathrm{MW}^{-1}$	$B_c = 20.9 \mathrm{kg} \mathrm{h}^{-1} \mathrm{MW}^{-1}$
	$C_c = -1.09 \mathrm{kg} \mathrm{h}^{-1}$	$C_c = -1.02 \mathrm{kg} \mathrm{h}^{-1}$	$C_c = -0.81 \mathrm{kg} \mathrm{h}^{-1}$
	$\underline{P}_c = 1.28 \mathrm{MW}$	$\underline{P}_c = 3.31 \mathrm{MW}$	$\underline{P}_c = 3.41 \mathrm{MW}$
R1	$B_c = 16.1 \mathrm{kg} \mathrm{h}^{-1} \mathrm{MW}^{-1}$	$B_c = 20.18 \mathrm{kg} \mathrm{h}^{-1} \mathrm{MW}^{-1}$	$B_c = 20.16 \mathrm{kg} \mathrm{h}^{-1} \mathrm{MW}^{-1}$
	$C_c = 8.39 \mathrm{kg} \mathrm{h}^{-1}$	$C_c = 0.83 \mathrm{kg} \mathrm{h}^{-1}$	$C_c = 0.88 \mathrm{kg} \mathrm{h}^{-1}$
	$\underline{P}_c = 1.92 \mathrm{MW}$	$\underline{P}_c = 4.37 \mathrm{MW}$	$\underline{P}_c = 4.48 \mathrm{MW}$
R2	$B_c = 21.08 \mathrm{kg} \mathrm{h}^{-1} \mathrm{MW}^{-1}$	$B_c = 21.02 \mathrm{kg} \mathrm{h}^{-1} \mathrm{MW}^{-1}$	$B_c = 18.72 \mathrm{kg} \mathrm{h}^{-1} \mathrm{MW}^{-1}$
	$C_c = -1.39 \mathrm{kg} \mathrm{h}^{-1}$	$C_c = -1.29 \mathrm{kg} \mathrm{h}^{-1}$	$C_c = 2.63 \mathrm{kg} \mathrm{h}^{-1}$
	$\underline{P}_c = 1.39 \mathrm{MW}$	$\underline{P}_c = 2.35 \mathrm{MW}$	$\underline{P}_c = 2.45 \mathrm{MW}$
R3	$B_c = 12.34 \mathrm{kg} \mathrm{h}^{-1} \mathrm{MW}^{-1}$	$B_c = 21.79 \mathrm{kg} \mathrm{h}^{-1} \mathrm{MW}^{-1}$	$B_c = 20.18 \mathrm{kg} \mathrm{h}^{-1} \mathrm{MW}^{-1}$
	$C_c = 9.64 \mathrm{kg} \mathrm{h}^{-1}$	$C_c = -2.35 \mathrm{kg} \mathrm{h}^{-1}$	$C_c = 0.28 \mathrm{kg} \mathrm{h}^{-1}$
	$\underline{P}_c = 1.28 \mathrm{MW}$	$\underline{P}_c = 1.38 \mathrm{MW}$	$\underline{P}_c = 4.48 \mathrm{MW}$

Table 7: Sizing and design parameters.

	Unit	Value	Description	Source
$V_{ m sto}$	$[m^3]$	200	Gas storage volume	
$V_{\rm sep}$	$[m^3]$	4	Separator volume	
$A_{ m el}$	$[\mathrm{m}^2]$	598	Electrochemical area	13
$A_{\rm s}$	$[m^2]$	131.56	Electrolyzer surface area	13
$A_{ m f}$	$[m^2]$	5.2×10^{-3}	Flow area in one cell	21
$A_{ m bf}$	$[m^2]$	1	Area of buffer tank	
$d_{ m m}$	[m]	5×10^{-4}	Membrane thickness	21
$d_{ m e}$	[m]	4.7×10^{-3}	Flow height	39
Δl	[m]	3	Hydrostatic height	
$C_{ m t}$	$[\mathrm{Jkg^{-1}}]$	51322.1	Stack thermal capacity	13
UHX	$[WK^{-1}]$	15210	Heat exchanger capacity	13
m_{cs}	[kg]	2602	Mass on cold side	40
$m_{ m hs}$	[kg]	1994	Mass on hot side	40
$n_{\rm c}$	[-]	230	Electrolyzer cell number	13

Table 8: Material and transport properties.

	Unit	Value	Description	Source
S_{H_2}	$[\text{mol kg}^{-1} \text{bar}^{-1}]$	8.84×10^{-5}	H ₂ solubility	41,42
S_{O_2}	$[\text{mol kg}^{-1} \text{bar}^{-1}]$	8.13×10^{-5}	O_2 solubility	$41,\!42$
$D_{ m H_2}$	$[m^2 s^{-1}]$	5.59×10^{-9}	H ₂ diffusion coefficient	4,43
$D_{\mathrm{O}_2}^{\mathrm{n}_2}$	$[m^2 s^{-1}]$	5×10^{-9}	O_2 diffusion coefficient	4,43
$Cp_{\mathrm{H}_2\mathrm{O}}$	$[J kg^{-1} K^{-1}]$	4186	H ₂ O heat capacity	13
Cp_1	$[J kg^{-1} K^{-1}]$	3101	Lye heat capacity	13
$ ho_{ m H_2O}$	$\left[\mathrm{kg}\mathrm{m}^{-3}\right]$	1000	H ₂ O density	
$\rho_{ m l}$	$\left[\mathrm{kg}\mathrm{m}^{-3}\right]$	1258.2	Lye density	40
σ	$[W m^{-2} K^{-4}]$	5.67×10^{-8}	Stefan-Boltzmann constant	
F	$[\mathrm{C}\mathrm{mol}^{-1}]$	96485.3	Faraday constant	
R	$[{ m J}{ m mol}^{-1}{ m K}^{-1}]$	8.314	Universal gas constant	
ϵ	[-]	0.8	Emissisivity constant	21
$h_{ m c}$	$[{ m W}{ m m}^{-2}{ m K}^{-1}]$	5.5	Convective heat transfer coefficient	21
γ	[-]	1.4	Heat capacity ratio	
$z_{ m H_2}$	[-]	2	H ₂ electron transfer number	
z_{O_2}	[-]	4	O_2 electron transfer number	
$M_{ m H_2}^2$	$[g \text{mol}^{-1}]$	2	H_2 molar mass	
$M_{\rm O_2}$	$[\operatorname{g} \operatorname{mol}^{-1}]$	32	O_2 molar mass	

Table 9: Parameters for U - I curves of stacks considered in this work. Dots indicate values that are the same for the degraded (stacks 2 and 3), and the novel stack 1.

	Unit	Stack 1	Stack 2	Stack 3
r_1	$[\mathrm{m}\Omega\mathrm{m}^2]$	2.18	2.62	2.84
r_2	$[\Omega \mathrm{m}^2^{\circ}\mathrm{C}^{-1}]$	-4.25×10^{-7}		
s	[mV]	117.9	141.5	153.3
t_1	$[{ m m}^2{ m A}^{-1}]$	-145.3×10^{-3}		
t_2	$[\mathrm{m}^2{}^\circ\mathrm{C}\mathrm{A}^{-1}]$	11.794		
t_3	$[{ m m}^2{}^{\circ}{ m C}^2{ m A}^{-1}]$	395.68		
f_1	$[{ m A}^2{ m m}^{-4}]$	1.2	1.44	1.56
f_2	[-]	0.98	0.97	0.96
κ	$[{ m S}{ m m}^{-1}]$	108		
K	$[{ m s}{ m m}^{-1}]$	137.74		
m	[-]	0.3	••	••

In Eq. 23 and below, the term $\dot{n}_{1,j}^{\rm in}$ denotes the incoming stream of dissolved species according to Eq. 2g and $\dot{m}^{\rm out,s}$ is the mass over the liquid outlet valve. In Eq. 25 we have used the assumption that the combined lye effluent of the stacks is equally distributed among both gasliquid separators. By cancelling terms we arrive at the form reported in Table 1.

C Implementation details

We present relevant implementation details regarding the valves, pressure drops, and controller tuning.

C.1 Valves and pressure drop

Remaining equations not presented in Table 1 pertain to pressure drops and actuator dynamics in the system. For simplicity, the following linear relationships are imposed to relate flow rates and pressure drops across the valves

$$\dot{m}_{\rm i} = z_{\rm i} k_{\rm i} \sqrt{\Delta} p \qquad \forall i \in \{1, 2, 3, 4, 7, 8\},$$
 (26)

$$\dot{n}_{i} = z_{i} k_{i} \sqrt{\Delta p} \qquad \forall i \in \{5, 6, 9\}, \tag{27}$$

where indices i denote the valve numbering as shown in Figure 1. The valve coefficients k_i are chosen to facilitate input usage over most of the operating range and are reported in Tab. 10. All valve openings and remaining actuator

positions follow first order dynamics

$$\frac{dz_{i}}{dt} = (z_{\text{ctr,i}} - z_{i})/\tau_{i} \quad \forall i \in \{1, 2, ...9, cw, U\}, \quad (28)$$

where indices cw and U denote actuator positions for the cooling water and the applied voltage, respectively. The control signal $z_{\text{ctr,i}}$ is applied to the valve positions z_i , following with a time constant of τ_i . This time constant is 1s for all actuators but the voltage, for which it is 0.01s. Generally speaking, the balance

Table 10: Overview of valve constants used in the model.

Index i	$k_{\rm i}$	Unit
1, 2, 3	8	${\rm kg}{\rm s}^{-1}{\rm bar}^{-0.5}$
4	0.3	$kg s^{-1} bar^{-0.5}$
5	8	$ m mols^{-1}bar^{-0.5}$
6	4	$ m mols^{-1}bar^{-0.5}$
7, 8	40	$kg s^{-1} bar^{-0.5}$
9	12	$ m mols^{-1}bar^{-0.5}$

of plant is a structure with height differences which have to be overcome by a pump to facilitate lye recirculation. It is herein assumed that the base of the gas-liquid separator stands at the height of the electrolyzers of $3 \, \mathrm{m}$. Neglecting friction losses, the pressure head p_1 to be overcome equals

$$\Delta p_{l} = \rho_{l} g \Delta l, \tag{29}$$

where Δl is the total hydrostatic height difference, i.e., considering liquid levels. The liquid pump pressurizes the liquid according to

$$P_{\text{pump}} = \sum_{k \text{in} \mathcal{K}} \dot{m}_{\text{lye}}^{\text{in},k} / \rho_{\text{l}}(p_{\text{HEX}} - p_{\text{bf}}), \tag{30}$$

where $p_{\rm bf}$ is the pressure in the buffer tank and $p_{\rm HEX}$ the pressure after the pump. For simplicity we assume a constant pump power $P_{\rm pump}$ of 5000 W.

C.2 Controller tuning

All controllers tuned in this work can be expressed through the following control law

$$u(t) = K_{\rm p} \Big(\beta r(t) - y(t) + \frac{1}{T_{\rm i}} \int_0^t e(\tau) d\tau \Big). \tag{31}$$

This is a general series PI controller with setpoint weighting for the proportional error through the parameter β . Setting $\beta = 1$ recovers the standard PI form, which is used for all controllers but those using integral reset (CC1 and CC4). For these, we set $\beta = 0$ to a) ensure that the controller output goes to zero when resetting the integral error, and b) to avoid potential overshooting (see also Sec. 3.1).

All PI controllers are tuned using SIMC tuning based on 5% input steps from steady-state operation on the undegraded system at 6 MW power. To achieve both good performance and robustness, controllers for integrating responses are tuned with the closed-loop time constant $\tau_{\rm c} = 3\theta_{\rm d}$, whereas those for first-order responses are tuned with $\tau_{\rm c}=2\theta_{\rm d}$. To avoid oscillations in the cooling water, the temperature controller TC4 is detuned by setting the integral time constant T_i to the process time constant. The controllers with integral reset are tuned with step responses starting at 1.5 MW to better capture the dynamics in the relevant low-load regions. For both we set $\tau_c = 5 \, \text{min}$ for a smooth but fast response. By setting

$$\tau_{\rm c,p^a} = \tau_{\rm c,p^c},\tag{32}$$

we detune the anode side pressure controller to match the time scale of the cathode side, which depends on the compressor.

References

- (1) Smolinka, T.; Bergmann, H.; Garche, J.; Kusnezoff, M. In *Electrochemical Power* Sources: Fundamentals, Systems, and Applications; Smolinka, T., Garche, J., Eds.; Elsevier, 2022; pp 83–164.
- (2) Electrolysis: a Norwegian success story. 2020; https://nelhydrogen.com/podcasts/electrolysis-a-norwegian-success-story/.
- (3) Dokso, A. Safety Issues and Efficiency Struggles Hit Sinopec's Kuqa Green Hydrogen Project - Energy News. 2023; https://tinyurl.com/52ncxtkt, Section: Projects.
- (4) Haug, P.; Koj, M.; Turek, T. Influence of

- process conditions on gas purity in alkaline water electrolysis. *International Journal of Hydrogen Energy* **2017**, *42*, 9406–9418.
- (5) Trinke, P.; Haug, P.; Brauns, J.; Bensmann, B.; Hanke-Rauschenbach, R.; Turek, T. Hydrogen Crossover in PEM and Alkaline Water Electrolysis: Mechanisms, Direct Comparison and Mitigation Strategies. *Journal of The Electrochemical Society* **2018**, *165*, F502–F513.
- (6) Qiu, Y.; Li, J.; Zeng, Y.; Zhou, Y.; Chen, S.; Qiu, X.; Zhou, B.; He, G.; Ji, X.; Li, W. Dynamic Operation and Control of a Multi-Stack Alkaline Water Electrolysis System with Shared Gas Separators and Lye Circulation: A Model-Based Study. 2025; http://arxiv.org/abs/ 2501.14576, arXiv:2501.14576 [math].
- (7) David, M.; Bianchi, F. D.; Ocampo-Martinez, C.; Sánchez-Peña, R. \mathcal{H}_{\min} Control periments for Increasing H2 Purity in High-Pressure Alkaline Electrolyzers. 2024 European Control Conference (ECC). Stockholm, Sweden, 2024; pp 2417 - 2422.
- (8) Uribe, J.; Santillan, E.; Camacho, O.; Ocampo-Martinez, C.; Aguirre, O. Sliding Mode Control Approach for H2 Purity Regulation in High-Pressure Alkaline Electrolyzers. *IFAC-PapersOnLine* **2024**, 58, 424–429.
- (9) Qi, R.; Gao, X.; Lin, J.; Song, Y.; Wang, J.; Qiu, Y.; Liu, M. Pressure control strategy to extend the loading range of an alkaline electrolysis system. *International Journal of Hydrogen Energy* **2021**, 46, 35997–36011.
- (10) Li, Y.; Zhang, T.; Deng, X.; Liu, B.; Ma, J.; Yang, F.; Ouyang, M. Active pressure and flow rate control of alkaline water electrolyzer based on wind power prediction and 100% energy utilization in off-

- grid wind-hydrogen coupling system. Applied Energy **2022**, 328, 120172.
- (11) Hu, S.; Guo, B.; Ding, S.; Tian, Z.; Gu, J.; Yang, H.; Yang, F.; Ouyang, M. Study on the synergistic regulation strategy of load range and electrolysis efficiency of 250 kW alkaline electrolysis system under high-dynamic operation conditions. eTransportation 2024, 19, 100304.
- (12) Cammann, L.; Jäschke, J. A simple constraint-switching control structure for flexible operation of an alkaline water electrolyzer. *IFAC-PapersOnLine* **2024**, *58*, 706–711.
- (13) Rizwan, M.; Alstad, V.; Jäschke, J. Design considerations for industrial water electrolyzer plants. *International Journal of Hydrogen Energy* **2021**, *46*, 37120–37136.
- (14) Shi, Y.; Hu, X.; Zhang, Z.; Lu, S.; Xie, L.; Su, H. Plant-wide Modeling, Design Consideration, and Practical Hierarchical Control Strategy Considering Key Variable Integral Characteristics for an Industrial Alkaline Water Electrolyzer Plant. Industrial & Engineering Chemistry Research 2023, 62, 14441–14455.
- (15) Chen, M.; Jia, J.; Zhang, B.; Han, L.; Ji, M.; Yu, Z.; Li, D.; Wang, W.; Jia, H.; Xu, H. Enhancing the Efficiency of Multi-Electrolyzer Clusters with Lye Mixer: Topology Design and Control Strategy. Energy Engineering 2024, 121, 3055– 3074.
- (16) Zheng, Y.; You, S.; Bindner, H. W.; Münster, M. Optimal day-ahead dispatch of an alkaline electrolyser system concerning thermal-electric properties and state-transitional dynamics. Applied Energy 2022, 307, 118091.
- (17) Liang, T.; Chen, M.; Tan, J.; Jing, Y.; Lv, L.; Yang, W. Large-scale off-grid wind power hydrogen production multi-tank combination operation law and scheduling

- strategy taking into account alkaline electrolyzer characteristics. *Renewable Energy* **2024**, *232*, 121122.
- (18) Li, X.; Gao, D.; Tang, J.; Lin, R.; Li, H.; Qi, R.; Sha, L.; Yang, C.; Li, W. Optimization of chemical engineering control for large-scale alkaline electrolysis systems based on renewable energy sources. *International Journal of Hydrogen Energy* 2024, 93, 193–206.
- (19) Skogestad, S. Control structure design for complete chemical plants. *Computers & Chemical Engineering* **2004**, *28*, 219–234.
- (20) Ulleberg, O. Modeling of advanced alkaline electrolyzers: a system simulation approach. *International Journal of Hydrogen Energy* **2003**, *28*, 21–33.
- (21) Cammann, L.; Perera, A.; Alstad, V.; Jäschke, J. Design and operational analysis of an alkaline water electrolysis plant powered by wind energy. *International Journal of Hydrogen Energy* **2024**, *93*, 963–974.
- (22) LeRoy, R. L.; Bowen, C. T.; LeRoy, D. J. The Thermodynamics of Aqueous Water Electrolysis. *Journal of The Electrochemical Society* **1980**, *127*, 1954–1962.
- (23) Vogt, H.; Balzer, R. The bubble coverage of gas-evolving electrodes in stagnant electrolytes. *Electrochimica Acta* **2005**, *50*, 2073–2079.
- (24) Eigeldinger, J.; Vogt, H. The bubble coverage of gas-evolving electrodes in a flowing electrolyte. *Electrochimica Acta* **2000**, 45, 4449–4456.
- (25) Skogestad, S.; Grimholt, C. In *PID Control in the Third Millennium*; Vilanova, R., Visioli, A., Eds.; Springer London: London, 2012; pp 147–175, Series Title: Advances in Industrial Control.
- (26) Raheli, E.; Werner, Y.; Kazempour, J. A conic model for electrolyzer scheduling. *Computers & Chemical Engineering* **2023**, 179, 108450.

- (27) Varela, C.; Mostafa, M.; Zondervan, E. Modeling alkaline water electrolysis for power-to-x applications: A scheduling approach. *International Journal of Hydrogen Energy* **2021**, *46*, 9303–9313.
- (28) Forsman, K.; Adlouni, M.; Skogestad, S. Split parallel control a little known control structure. *IFAC-PapersOnLine* **2025**, 59, 552–557.
- (29) Skogestad, S. Advanced control using decomposition and simple elements. *Annual Reviews in Control* **2023**, *56*, 100903.
- (30) Wächter, A.; Biegler, L. T. On the implementation of an interior-point filter linesearch algorithm for large-scale nonlinear programming. *Mathematical Programming* **2006**, *106*, 25–57.
- (31) Lubin, M.; Dowson, O.; Garcia, J. D.; Huchette, J.; Legat, B.; Vielma, J. P. JuMP 1.0: Recent improvements to a modeling language for mathematical optimization. 2023; http://arxiv.org/abs/2206.03866, arXiv:2206.03866 [cs].
- (32) Ma, Y.; Gowda, S.; Anantharaman, R.; Laughman, C.; Shah, V.; Rackauckas, C. ModelingToolkit.
- (33) Nord Pool | Day-ahead prices. https://data.nordpoolgroup.com/auction/day-ahead/prices?deliveryDate=latest¤cy=EUR&aggregation=DeliveryPeriod&deliveryAreas=NO3.
- (34) Johnsen, A. G.; Mitridati, L.; Zarrilli, D.; Kazempour, J. The Value of Ancillary Services for Electrolyzers. 2025; http://arxiv.org/abs/2310.04321, arXiv:2310.04321 [math] version: 4.
- (35) Cammann, L.; Alves, E. F.; Jäschke, J. Dynamic minimum loads for FCR market participation of alkaline water electrolyzers. IECON 2024 50th Annual Conference of the IEEE Industrial Electronics Society. 2024; pp 1–6.

- (36) Baumhof, M. T.; Raheli, E.; Johnsen, A. G.; Kazempour, J. Optimization of Hybrid Power Plants: When is a Detailed Electrolyzer Model Necessary? 2023 IEEE Belgrade PowerTech. 2023; pp 1–10.
- (37) Zheng, Y.; You, S.; Bindner, H. W.; Münster, M. Incorporating Optimal Operation Strategies into Investment Planning for Wind/Electrolyser System. *CSEE Journal of Power and Energy Systems* **2022**, *8*, 347–359.
- (38) Guo, H.; Zhang, C.; Wang, J.; Wu, Z.; Wang, T.; Wang, P.; Qian, Y.; Zhang, G.; Yu, F. Design and operation schedule of RES hydrogen production system with downstream constraints. *International Journal of Hydrogen Energy* **2025**, 102, 68–79.
- (39) Sakas, G.; Ibáñez-Rioja, A.; Ruuskanen, V.; Kosonen, A.; Ahola, J.; Bergmann, O. Dynamic energy and mass balance model for an industrial alkaline water electrolyzer plant process. *International Journal of Hydrogen Energy* **2022**, 47, 4328–4345.
- (40) Rizwan, M. Plantwide control of alkaline water electrolyzer plant for hydrogen production. M.Sc. thesis, NTNU, 2020; Accepted: 2021-09-28T18:23:25Z ISSN: 3449-6807.
- (41) Knaster, M.; Apel'Baum, L. Solubility of hydrogen and oxygen in concentrated potassium hydroxide solution. https://www.scopus.com/record/display.uri?eid=2-s2.0-0040465647&origin=inward&txGid=b84c6320664ae9604e3730c7d843bc33.
- (42) Allebrod, F. High Temperature and Pressure Alkaline Electrolysis.
- (43) Tham, M. J.; Walker, R. D. J.; Gubbins, K. E. Diffusion of oxygen and hydrogen in aqueous potassium hydroxide solutions. *The Journal of Physical Chemistry*

 $\mathbf{1970},\ 74,\ 1747-1751,\ Publisher:\ American Chemical Society.$

Graphical abstract:

